A winter storm in Alderney Race: Impacts of 3D wave–current interactions on the hydrodynamic and tidal stream energy

Anne-Claire Bennis, Lucille Furgerot, P. Bailly Du Bois, Emmanuel Poizot, Yann Méar, F. Dumas

A winter storm in Alderney Race : impacts of 3D wave-current interactions on the hydrodynamic and tidal stream energy

A.-C. Bennis *[1], L. Furgerot[1,2], P. Bailly Du Bois[3], E. Poizot[3], Y. Méar[3], and F. Dumas[4]

[1]UNICAEN, CNRS, UNIROUEN, UMR 6143 M2C, 24 rue des Tilleuls, 14000 Caen, France
[2]Energie de la Lune, 87 Quai de Queyries, 33100 Bordeaux, France
[3]UNICAEN, EA 4253 LUSAC, 60 rue Max-Pol Fouchet, 50130 Cherbourg en Cotentin, France
[4]Shom, STM/REC, 13 rue du Chatellier, 29200 Brest, France

*corresponding author : A.-C. Bennis, Normandie Univ., UNICAEN, CNRS, UNIROUEN, Morphodynamique Continentale et Côtière (M2C), 24 rue des Tilleuls, 14000 Caen, France. Email : ac.bennis@unicaen.fr. Phone : +33.2.31.56.57.18. Fax : +33.2.31.56.57.57.

Abstract

Due to the climate change, it is necessary to modify the energy modes of production. The mix energetic, based on renewable energies as tidal currents, is one of the solutions to decrease the energy production carbon footprint. This article focuses on hydrodynamic interactions in Alderney Race (France), which is the most energetic tidal site in Western Europe with a maximum potential of 5.1 GW according to Coles et al. (2017). The impact of a winter storm occurring during spring tide is assessed thanks to numerical modeling with a 3D fully-coupled wave-current model and in-situ data. This study starts to analyze the impacts of the storm on the wave field and the current effects on waves. Then, the modifications of the current and tidal stream energy caused by waves are discussed. After a successfull validation step with excellent PBIAS and R^2 scores, the main finding are : i) although the current intensity is strong (around 3-4 $m.s^{-1}$), the wave action significantly changes the vertical profile of the current, with a reduction of the PBIAS by a factor of 1.78 between simulations with and without wave effects, ii) ocean waves affect the tidal assymmetry, with a flood current whose intensity is 13% higher than for the ebb current, inducing a decrease of 30% in the tidal stream energy, iii) the flow is very sensitive to the angle between the directions of propagation of waves and current, with an acceleration or a reduction of the velocity, as observed in the presence of a 3D turbulent structure, iv) current effects on waves cause a wavenumber shift, changes in significant wave height (modulated by tide), wave direction due to refraction and an increase of the energy transfer from waves to ocean ascribed to the wave breaking. By a feedback mechanism, the modifications of the wave field by current and water level significantly alter the flow with a decrease of its velocity when waves propagate against current. This study shows that the 3D wave-current interactions need to be considered during a storm even during a spring tide event where currents are the strongest.

Keywords— Marine renewable energy, tidal sea, winter storm, wave-current interactions and coupling, three-dimensional numerical modeling, tidal energy estimate, Alderney race

1. Introduction

In its last report, the Intergovernmental Panel of Climate Change (IPCC [1]) highlights again on the necessity for human activities to reduce its greenhouse gas emissions. Nowadays, 70% of the world electric production is based on fossil energy consumption (natural gas, oil and coal). Solar and wind farms are in a high development rate, but cannot provide for all the needs on their own, in the context of a growing demand. Every alternatives to classical electricity product modes have to be investigated, in which tidal farms. Companies exploiting tidal energy are interested in tidal sites where the depth is less than 50 m and the maximum tidal current is larger than $2.5\,\mathrm{m.s^{-1}}$ (e.g. Lewis et al. 2015). Once the sites have been selected, they are subjects to a more detailed resource characterisation according the IEC 62600 standard. Then, it is necessary to identify the factors that could affect this resource (e.g. interactions between hydrodynamic processes, marine turbulence, sediment transport).

The Alderney Race (hereinafter referred as AR) (English Channel, France) is the third strongest tidal currents place of the world, the first in western Europe with current speed of up to $5\,\mathrm{m.s^{-1}}$ during high spring-tide. This site, with a maximum potential of 5.1 GW which exceeds the estimate for the Pentland firth by 35% (Coles et al. 2017), is very interesting for the exploitation of its current resource and many works have been conducted there (e.g. Mercier et al. 2021; Bennis et al. 2021; Thiébaut et al. 2020). Authors have shown a high variability and level of turbulence along the water column and on the bottom due the interactions between the flow and the seabed morphology, which could have an impact on the resource. However, despite the recent efforts to measure this turbulent activity, difficulties still remain in evaluating turbulent structures, particularly near the bottom, as reported by Mercier et al. (2021). In parallel, innovative numerical modelings (e. g. Bennis et al. 2021; Mercier et al. 2020), based on Large Eddy Simulation (hereinafter referred as LES) methods, were developed in order to help the understanding of the near-bed turbulent motions.

Wave-current interactions (hereinafter referred as WCI) are also an important point for the design of tidal converters, especially concerning the fatigue due to the vertical shear of the current that they cause. This topic was addressed in the framework of the HYD2M program [2]. WCI were studied using *in-situ* and High-Frequency (hereinafter referred as HF) radar measurements as well as by the use of numerical models. Cross-comparisons were carried out. The one-year of *in-situ* data have revealed that wave effects were absent during only 6% of the time from june 2017 to july 2018 (i.e. significant wave height (Hs) less than 0.5 m and wind speed lower than $4\,\mathrm{m.s^{-1}}$ during 22 days over 365 days) as reported in Furgerot et al. (2020). This shows that most of the time it is necessary to consider wave effects in studies. Strong vertical shears due to waves (Stokes drift and wave-breaking

1. https ://www.ipcc.ch/srocc/
2. HYD2M was funded by ANR (ANR-10-IEED-0006-07) for the building of France Energies Marines.

turbulence) have been measured in the upper-half of the water column. In the same time, wave effects change both bottom friction and turbulence. As a result, the flow velocity is affected throughout the water column due to waves. Concerning the horizontal shear of the current, which is difficult to determine using Acoustic Doppler Current Profiler (hereinafter referred as ADCP), HF radars have allowed to improve its knowledge. Despite the good accuracy of the surface current measures with HF radar (Lopez et al. 2020), the strong tidal current in AR induces a high level of noise in the doppler spectra making difficult an accurate determination of the sea state characteristics. As reported by Lopez et al. (2018) and for the moment, only the sea state characteristics recorded when the tidal current velocity is around $1\,\mathrm{m.s^{-1}}$ or less, are coherent to the ADCP data. In parallel, three-dimensional (hereinafter referred as 3D) numerical modeling of the hydrodynamic in AR has shown different effects ascribed to WCI. These effects are described in Bennis et al. (2020) for different sea conditions (ie. slightly to rough conditions according to the Douglas sea scale) : i) the flow velocity is decreased/increased in the upper half of the water column depending on the angle between the directions of propagation of waves and current according to the mechanism pointed out by Groeneweg and Klopman (1998), ii) ocean waves are deviated from their initial direction due to the interactions with surface current which causes wave refraction, iii) the enhancement of the bottom friction caused by waves results in a reduction of the tidal current velocity and tidal stream energy, iv) the turbulent mixing, particularly near the surface, is changed ascribed to the wave breaking induced by WCI. The study carried out in Bennis et al. (2020) was the first one to simulate and analyze the WCI effects in 3D for AR. Pioneer studies have been carried out for other tidal sites and for idealized conditions. For example, Guillou et al. (2016) have used 3D radiation stresses, that were constant over the depth, to simulate WCI in the Iroise sea (Brittany, France) for an application to the Fromveur tidal site. Another example is the work of Hashemi et al. (2015) where they have computed the barotropic (2D) wave-induced flow at the tidal site off the north-western coast of Anglesey Islands (Wales, UK).

Therefore, few studies have been conducted on the WCI and to our knowledge, the 3D effects induced by a winter storm on hydrodynamic and tidal stream energy have not yet been studied nor published for AR. This paper continues the researches initiated by Bennis et al. (2020) by assessing the impacts of the Eleanor's storm (2-5 January 2018) with the 3D-fully coupled wave-current model (MARS3D-WWIII) and *in-situ* data from wave buoy, ADCP and wind anemometers. It focuses on the role of ocean waves in this high-energy tidal environment targeted for the installation of tidal turbines, through a spatial analysis of the hydrodynamic processes.

The manuscript is organized as follows. After a short introduction in section 1, the methodology, including a description of the study site, data, numerical modeling platform,

and experiments, is presented in section 2. Then, results are shown and discussed in section 3. After a validation step, achieved through cross-comparisons, the spatialized hydrodynamic in AR is commented, particularly in the light of WCI. Conclusions are dressed in section 4.

2. Methodology

a. Study Site

The study site is located in the English Channel (EC) separating United Kingdom from France. EC is a shallow epi-continental sea, where the maximum depth of 174 m is reached in the Hurd Deep (150 km in length and 1.5 to 5 km in width). Semidiurnal tides, with a period of 12 h and 24 min, dominates the tidal regime in EC. Along the French coast and mainly in the Mont-Saint-Michel Bay, the tidal range is the greatest of all EC reaching 15 m. The tidal residual, propagating from the western to the eastern EC, combined with average south-westerly winds generates a water replacement time varying from 200 to 500 days, with longer residence times associated with residual currents gyres in coastal areas and gulfs as the Britany Isles area (Salomon and Breton 1993). Due to the Coriolis force, current velocities are higher along the French coast than the English coast, reaching greater than 1.5 $m.s^{-1}$ in north Brittany and exceeding 4 $m.s^{-1}$ off the Cotentin Peninsula. Turbulent gyres are found around the Channel Islands and also near the capes of Fréhel, Barfleur, Antifer, and Gris Nez. More details related to EC are available in Raoux et al. (2021); Dauvin (2019), for example.

Our EC study site is Alderney Race (AR), which is placed off the Cotentin Peninsula between the La Hague cape and the Alderney island (Fig. 1). The depth in AR varies between 25 m and 90 m. The tidal current can exceed 5 $m.s^{-1}$ during spring tides due to a conservation of mass effect that accelerates the tidal flow. Furgerot et al. (2020) have reported an instantaneous flow velocity of 7 $m.s^{-1}$ in exceptional conditions. The mean spring tidal ranges from 6 to 10 m from north to south of the La Hague cape ; A tidal asymmetry occurs between the ebb and flood tides ascribed to the relationship between the tidal constituents (Bailly du Bois et al. 2012, 2020). Wind-waves and swell propagate most of the time from west to east and crossed seas are observed. Rough seas are also seen in AR with ocean waves of a wavelength smaller than 50 m. Highly energetic 3D turbulent structures live in AR (e.g. Mercier et al. 2021; Furgerot et al. 2020) that have a length scale of a few tens of meters. The AR sea bottom is very rough and uneven with different geologic features like submarine cliffs (Furgerot et al. 2019). Strong hydrodynamic interactions (e.g. bottom-flow interactions, wave-current interactions) occur in AR as reported in many studies (e.g. Bennis et al. 2018, 2020; Bourgoin et al. 2020; Furgerot et al. 2020; Mercier et al. 2020). However, some efforts are still required to understand the hydrodynamic processes during a winter

storm. We choose to study the Eleanor's storm (2-5 January 2018) for which ADCP data are available. As tidal companies would like to install pilot and commercial tidal farms off Goury to have an average flow velocity around $2\,\mathrm{m.s^{-1}}$ (Fig. 1, black polygon), the hydrodynamic and WCI in this area will be discussed in details in section 3.

b. Data Collection

ADCP data were collected by the HYD2M consortium in 2018 (Furgerot et al. 2020), using a bottom-mounted 500 kHz Teledyne RDI Sentinel V50 (Fig. 1, red star). ADCP was located at $49°40'50.00''\,\mathrm{N}/2°01'46.44''\,\mathrm{W}$. The position of the ADCP was chosen to minimize the risks of damage (shock, loss, and bottom trawling) while having strong tidal current to characterize hydrodynamic interactions. The size of the measuring cells (bin) was 1 m with the first cell located at 2 m above the seabed. The wave parameters were estimated from ADCP measurements (20-min burst at 2 Hz every hour) and more specifically from the wave orbital velocity and the surface tracking (or direct echolocation of surface) algorithms (RDI 2017; Strong et al. 2000). For the selected time period and at the ADCP position, the significant wave height is higher than 4 m about 35% of the studied time period (very rough sea, Douglas sea scale), the wave period is ranging $7 - 11\,\mathrm{s}$ and waves come from the west sector (between 220 and 300°). The velocity data were 10 minutes averaged to compare with numerical simulations and reach $3.5\,\mathrm{m.s^{-1}}$ during flood time period. The flow direction is oriented towards north-east and south-west for flood and ebb, respectively. At this place and time, tidal range varies from 7 to 8 m with a mean depth of 35 m. Data from Met-Office wave buoy (62103), available on EMODnet platform (http ://www.emodnet.eu), were also used for comparison with the wave model results. Wind measurements at the Goury semaphore have been tested against the numerical wind forcings from Météo-France.

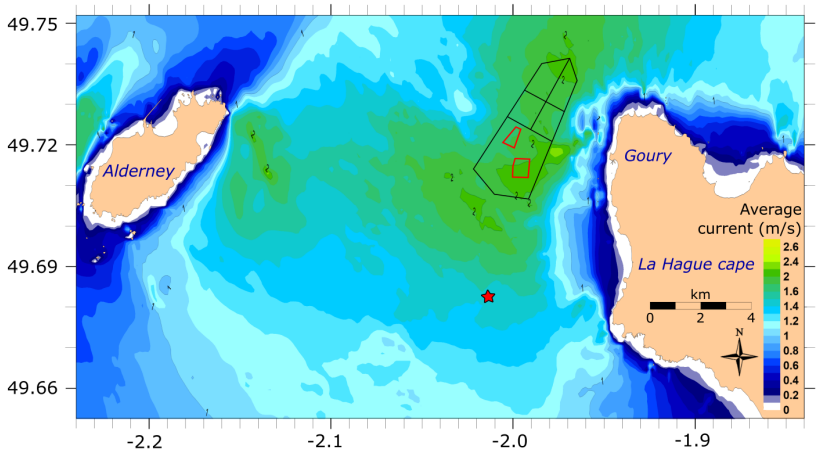

FIGURE 1: Study site (AR) located between the Alderney island (land on the left) and the French coast (land on the right). The black polygon represents the appropriate area for future tidal farms. The red areas have been specifically selected for two proposed tidal projects. ADCP location is represented by a red star. The time and depth average flow velocity is superimposed in colored contours according to Bailly du Bois et al. (2020).

c. *Numerical modeling*

The three-dimensional hydrodynamical model, MARS3D v10 (hereinafter referred as MARS, Lazure and Dumas 2008), is used in combination with the spectral wave model, WAWEWATCH-III v4.18 (hereinafter referred as WWIII, Tolman and al. 2014) to simulate the flow motions under the wave action. MARS computes the flow dynamic under wave, wind and tide actions. WWIII is a spectral wave model that simulates generation, propagation and dissipation of ocean waves by solving the wave action equation (more details in Tolman and al. 2014). For MARS simulations, wave forcing is based on the set of equations of Ardhuin et al. (2008) and Bennis et al. (2011). All details regarding the equations and their implementations are available in Bennis et al. (2011, 2014, 2016, 2020). In the light of the numerous papers describing the sets of equations, they are not detailed here but briefly overviewed.

The generic formulation of momentum equations for a wave-forced, three-dimensional, incompressible, unsteady, hydrostatic, constant-density flow is :

$$\frac{\mathrm{D}\widehat{\mathbf{U}}}{\mathrm{Dt}} = \mathbf{S_{EPG}} + \mathbf{S_{VM}} + \mathbf{S_{HM}} + \mathbf{S_{WP}} + \mathbf{S_{BA}} + \mathbf{S_{BBL}} + \mathbf{S_{VF}}, \quad (1)$$

where $\widehat{\mathbf{U}} = (\widehat{U}, \widehat{V}, \widehat{W})$ is the 3D quasi-Eulerian velocity defined as the Lagrangian velocity minus the Stokes drift. The source terms $\mathbf{S_{EPG}}$, $\mathbf{S_{VM}}$, $\mathbf{S_{HM}}$, $\mathbf{S_{WP}}$, $\mathbf{S_{BA}}$, $\mathbf{S_{BBL}}$, $\mathbf{S_{VF}}$ are related to the external pressure gradient, the vertical mixing, the horizontal mixing, the

wave-induced pressure gradient, the breaking acceleration, the bottom streaming, the vortex force, respectively. This set of equations is compatible with that of McWilliams et al. (2004) used in Uchiyama et al. (2010), Kumar et al. (2012) and Marchesiello et al. (2015), for example.

The wave forcing, based on the vortex force formalism applied to the mean flow, consists to add wave forcing terms to the primitive equations of the ocean allowing to take into account the effects of the wave-induced pressure, the Stokes drift, the wave breaking acceleration, the wave-induced turbulent mixing and the redistributing of the momentum via the vortex force. The well-known turbulent closure, $k - \epsilon$, for vertical mixing is also adapted to include wave-induced source terms of turbulent kinetic energy (k) and dissipation (ϵ) according to Walstra et al. (2000) (more details in Bennis et al. 2014). Boundary conditions for the flow velocity, sea surface height and turbulent quantities are also changed (more details in Bennis et al. 2011, 2020). The coupling between MARS and WWIII is managed by the automatic coupler OASIS developed by CERFACS (Valcke et al. 2015) and is two-way (Bennis et al. 2020). Thus, we are able to simulate the modifications of the flow ascribed to waves and also the changes in the wave field due to the interactions with surface current and sea surface height.

d. Numerical configuration and experiments

The horizontal computational grids of MARS and WWIII are similar with an horizontal resolution of 600 m and it covers the spatial domain going from 47°53′60.0″ N / 6°03′32.4″ W to 50°27′0.0″ N / 0°43′12.0″ W (Fig. 2). Even if simulations for Alderney Race at finer resolutions (120 m) compared with in-situ data (Bennis et al. 2020) highlighted very good agreements, we selected a low spatial resolution in order to : 1) be able to compare numerical results with HF radar data at 750-m of radial resolution in the future and, 2) reduce the computing time. Moreover, it is interesting to know if the model is accurate and relevant for a such spatial resolution. MARS simulations are three-dimensional with 25 sigma levels evenly distributed over the vertical. The tidal forcing of MARS is based on the Shom CST France atlas that includes 114 tidal components (Leroy and Simon 2003). MARS is forced by the wave forcing terms computed by WWIII (Eq. (1) and more details in Bennis et al. 2011). WWIII uses 32 frequencies from 0.04 Hz to 0.7678 Hz and 24 directions leading to a directional step of 15°. WWIII is constrained at its open boundaries by bi-dimensional (frequency-direction) wave energy spectra from the HOMERE and Ifremer databases (Boudiere et al. 2013). According to the coupling mode, WWIII is forced by surface current and water level computed by MARS. Wind at 10-m height above the sea from the Meteo-France re-analysis (ALADIN atmospheric model) is used to force MARS and WWIII at the surface. The coupling time step is 20 s, which is greater than or equal to the model time steps (i. e. 4 s

for MARS3D and 20 s for the global time step in WWIII). Details of numerical experiments are summarized in Table 1 and presented in Fig. 3.

Four numerical configurations are tested against data : i) Run A including wind and tide effects, ii) Run B taking into account only tide effects and iii) Runs C and D integrating tide, wind and wave effects for two different coupling modes. Run C uses a two-way wave-current coupling (ie. current and water level effects on waves are considered) while Run D is one-way (ie. current and water level effects on waves are NOT considered).

	Tide effects	**Wind effects**	**Wave effects**	**Wave-current coupling**
Run A	X	X	-	no
Run B	X	-	-	no
Run C	X	X	X	yes, TW
Run D	X	X	X	yes, OW

TABLE 1: Description of the four numerical simulations (Runs A, B, C and D) according the forcing fields (tide, wind and waves). TW (with current and water level effects on waves) and OW (without current and water level on waves) represent the two-way and one-way coupling modes, respectively.

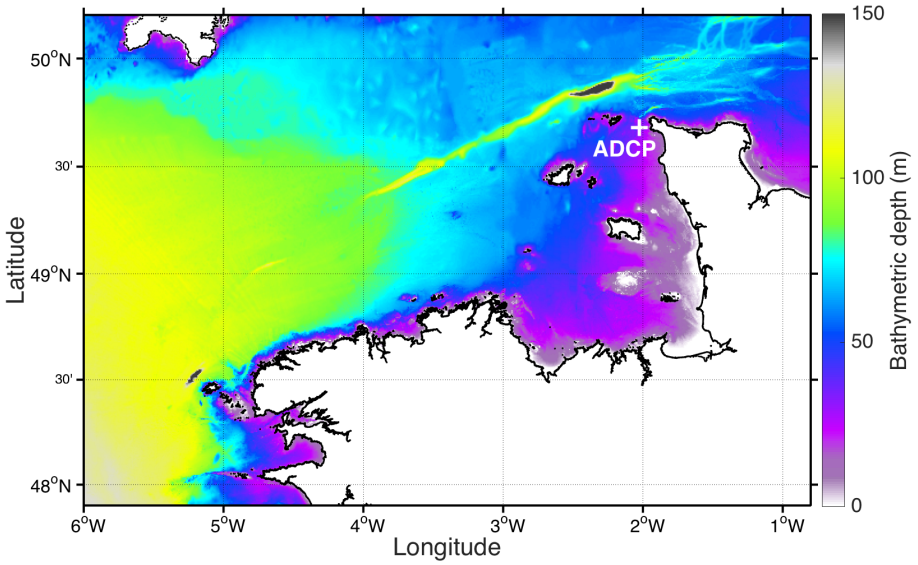

FIGURE 2: Bathymetric map (LAT, source : Shom) and spatial dimensions of the horizontal grids of MARS and WWIII. The ADCP location is drawn with a white cross.

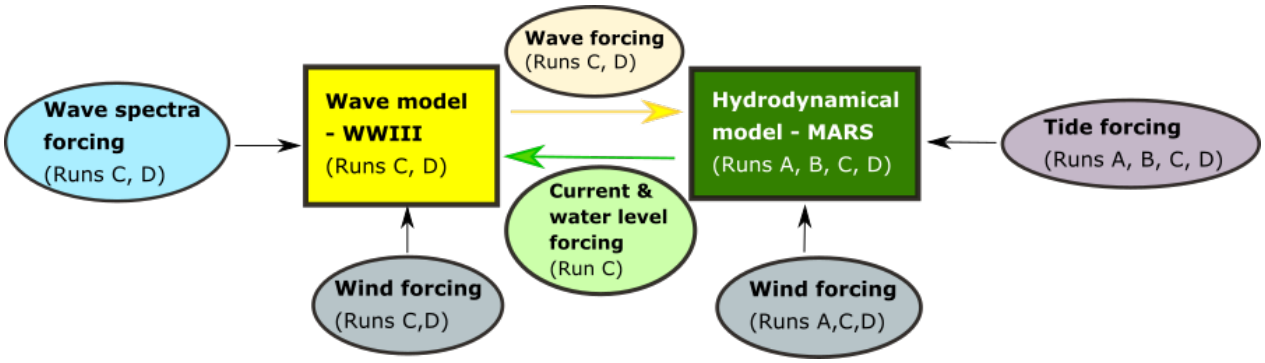

FIGURE 3: Schematic representation of the forcings involved in the numerical modeling according to the test cases (Runs A, B, C, D).

Model accuracy is evaluated through the root mean square error (RMSE), normalized root mean square error (NRMSE), BIAS, PBIAS and R-squared (R^2), such as (e.g. Allen et al. 2007b,a) :

$$\mathrm{RMSE} = \sqrt{\frac{\Sigma(X_{model} - X_{data})^2}{N}}, \tag{2}$$

$$\mathrm{NRMSE} = \frac{\mathrm{RMSE}}{\max(X_{data}) - \min(X_{data})}, \tag{3}$$

$$\mathrm{BIAS} = \frac{\Sigma(X_{model} - X_{data})}{N}, \qquad |\mathrm{PBIAS}| = 100 \text{ x } |\mathrm{BIAS}|, \tag{4}$$

$$\mathrm{R}^2 = 1 - \frac{\Sigma(X_{data} - X_{model})^2}{\Sigma(X_{data})^2}, \tag{5}$$

where N is the total number of available samples (120). X_{model} and X_{data} represent the samples coming from numerical simulations and in-situ data for 1-5 January 2018, respectively. PBIAS allows us to know if the model is systematically underestimating or overestimating the measurements. $|\cdot|$ denotes the absolute value operator. The closer the value is to zero the better the model. Some categories were defined to estimate the performance levels regarding $|\mathrm{PBIAS}|$: ≤ 10 excellent, $10-20$ very good, $20-40$ good, ≥ 40 poor (Marechal 2004; Allen et al. 2007a). R^2 is a statistical measure to quantify dispersion around a fitted regression line, with a perfect fit for $\mathrm{R}^2 = 1$. R^2 performance levels were defined as : ≥ 0.65 excellent, $0.65-0.5$ very good, $0.5-0.2$ good, ≤ 0.2 poor (Marechal 2004). The ranges chosen to categorize the performance levels are subjective. They are solely used for evaluating the performances of our numerical model in four categories from excellent to poor.

3. Results and Discussion

In this section and after a validation step, the spatialized hydrodynamic of AR during the Eleanor's storm is analyzed with a special interest in the area selected for implementation of tidal turbines (Fig. 1, black polygon). Sea states and wind are first described and discussed. Then, we focus on the flow velocity and tidal stream energy.

a. Sea States and wind

During the studied period, the Eleanor's storm generated strong wind in EC. The anemometers at the 62103 wave buoy and Goury Semaphore recorded a wind velocity about $20\,\mathrm{m.s^{-1}}$ around 4 a.m. on 3 January 2018 (Fig. 4d). The wind velocity continued to increase at the buoy location until it reached a maximum value of $25\,\mathrm{m.s^{-1}}$ around 7 a.m. on 3 January 2018 (Fig. 4d, black circles). In contrast, a different behavior was observed in Goury where the wind velocity decreased slightly after 4 a.m. on 3 January 2018 (Fig. 4d, blue circles).

The storm was coming from the Atlantic Ocean with a wind blowing from the west, with a direction around 270° (Fig. 4e). The storm energy decreased during its propagation in EC from west to east, explaining the weaker wind velocity in Goury. A very good agreement is found between the wind data, from the buoy and Goury Semaphore, and the numerical wind forcings from ALADIN, respectively with an NRMSE of 0.13 and 0.16, a |PBIAS| of 9.22% and 14.59% and a R^2 of 0.96 and 0.95 (Table 2). Main differences are likely due to the coarse horizontal resolution (around 7.5 km) of the ALADIN model and the output time step of 6 hours which does not allow to simulate the impacts of the hourly variations of the wind. Moreover, NRSME and |PBIAS| are stronger at Goury than at the buoy position. That is probably caused by the land location of the Goury Semaphore, that generates different turbulent motions in the atmospherical boundary layer. As the wind generates sea states by moving the sea surface, ocean waves and wind at 10-m height are correlated. As a result the time evolution of the significant wave height (Hs, Fig. 4a) follows the time evolution of the wind most of the time (Fig. 4c). Maximum values of Hs and of the wind velocity occurred at the same time, on the mornings of the 3 and 4 January. The Hs of 7.5 m on 3 January at 7 :15 a.m. estimated from ADCP is difficult to explain because it is inconsistent with wind data recorded by the Goury Semaphore (Fig. 4d, blue circles). This Hs was calculated with an algorithm based on the wave orbital velocity. Using another algorithm based on the surface tracking method (Fig. 4a, light blue crosses), the post-processed Hs is similar to that calculated by the wave orbital velocity method except for the highest Hs values on 3 and 4 January. In particular, a Hs around 4 m is observed on 3 January at 7 :15 a.m, which is closer to the numerical results. The differences between the Hs post-processed by the two

algorithms occur when the tidal current is strongest. It is possible that the algorithm using the wave orbital velocity method has some difficulty separating the wave orbital velocity from the tidal current when this latter is strong. Further investigations are needed to clarify this situation. However, as the flow response to wave effects is consistent with the ADCP data (Section 3b), the simulated Hs should not be too far from the real Hs and the values calculated by the surface tracking method appear more realistic.

Despite this problem, statistics for Hs computed over 5 days have revealed excellent scores with with a |PBIAS| of 7.42% and 1.78 % at the wave buoy and ADCP locations, respectively, and an NRMSE lower than 0.24 (Table 2). The dispersion of the model data is excellent with values of R^2 around 0.93. Very good scores are also obtained for wave period and direction (Table 2). When the surface tracking method is used, the lowest wave periods (around 4 s) disappear from the post-processed data (Fig. 4b, light blue crosses), improving the fit to the numerical results. These low values correspond to the highest values of Hs discussed before, showing that the wave orbital velocity algorithm also generates spurious values for wave period for a strong tidal current. Changes in wave direction inducing wave motions towards the northeast during the ebb and towards the southeast during the flood ascribed to wave refraction by currents were also well reproduced for this period (Fig. 4e), following the conclusions of Bennis et al. (2020); Ardhuin et al. (2012).

The impacts of the surface current and water level on the wave field are presented on maps Fig. 6 through the relative difference (Δ) defined as :

$$\Delta R = 100 \cdot \left(\frac{R_{tw} - R_{ow}}{R_{ow}} \right), \tag{6}$$

where ΔR stands for the relative difference related to the R parameter. R_{tw} and R_{ow} represent the value of R produced by Run C and D, respectively.

To ease the analysis, 3 zones were defined on the map Fig. 5a (#W1 La Hague point, #W2 northern part of the peninsula and #W3 south part) for which we will comment the dynamic. Results of Run C (with current and water level effects on waves) and D (without current and water level effects on waves) are compared by this mean for the significant wave height (ΔHs), the wave direction (ΔDir) and the mean wavelength (ΔLm). The dynamic was particularly studied for three time points (T0, T1 and T2), for which the flow velocity is maximum (Fig. 7). T0, T1 and T2 are on 3 January at 1 :15 a.m. (low tide), 7 :15 a.m. (high tide) and 2 :15 p.m. (low tide), respectively. At high tide (T1) an increase in Hs (i.e. $\Delta \mathrm{H_s} > 0$ and red color on map Fig. 6) of about 20% due to tidal effects was observed in #W1 (Fig. 6d) and anywhere else a decrease (i.e. $\Delta \mathrm{H_s} < 0$ and blue color on map Fig. 6). In #W1, as shown in Fig. 5b, e, the angle between wave and current directions of propagation (θ_{wc}) is large ($\geq 110°$) and the current velocity is very high ($\simeq$ 3-4 $\mathrm{m.s^{-1}}$), explaining high positive values of $\Delta \mathrm{H_s}$. The enhancement of waves, leading to higher waves, when waves

propagate against current is already well documented (e.g. Wang and Sheng 2018; Guillou 2017) and it is observed here. Due to the same mechanism, at low tide (T0, T2) an increase in Hs in #W2 (Fig. 6a,g) was caused by large θ values reaching almost 180° (Fig. 5a,c,d,f). In contrast, a decrease in the south part of the domain (#W3) for the three time points has been generated by orthogonal waves and current. It is noticeable that near the coast at T2 where the tidal current is weak ($\leq 1\,\mathrm{m.s^{-1}}$) the Hs is significantly affected by tide with a reduction around 15%. Otherwise, the variations of the wave to ocean energy flux (Foc) ascribed to tidal effects on waves were coherent with the Hs variations. When Hs is increased, wave breaking occurred and then wave energy is transmitted to the water column, that produces positive values of ΔFoc (not shown here).

Another well-known tidal effect on sea states is the change in the wave direction due to the refraction phenomenon caused by tidal current. At high tide (T1) and low tide (T0, T2) two different behaviors were observed (Fig. 6 b,e,h) : i) the flood current, propagating towards the northeast during high tide, deviates waves towards the southeast, that corresponds to positive values of ΔDir (in red), ii) the ebb current at T0 and T2, which is oriented southwest at low tide, brings waves towards the northeast, that is represented by negative values of ΔDir (in blue).

Moreover, tidal currents generate a wavenumber shift producing variations into wavelength and intrinsic wave frequency, leading to modifications of the wave velocity and changes in Hs (e.g. Wang and Sheng 2018; Draycott et al. 2018). Thus, when Hs is enhanced due the action of an opposing current, wavelength is reduced, and vice versa. That was mainly observed in #W3 at T0 and T2, in #W2 off the coast at T2, in #W1 at T1 and T0 (Fig. 6 c,f,i). At the ADCP position, the tidal modulation of the wavelength is weak (Fig. 8b, gray dashed and solid lines). However, at other locations (e.g. 49°42′29.88″N-2°6′5.40″W) as presented in Fig. 8a, b, the tidal modulation is clearly visible for all tidal cycles with a decrease and an increase in wavelength during the ebb and flood, respectively.

Frequency wave-energy spectra show a modulation of the energy during the tidal cycle because of the wave-current interactions (Fig. 9). Indeed, at T0 − 30′, T0, T0 + 1h30′, tidal current flows towards the southwest and causes an enhancement of the wave energy (Fig. 9a,b,c). The peak of energy is around 0.12 Hz that corresponds to a wave period (T_{0m-1}) around 8.3 s which is characteristic of wind-sea. For frequencies higher than 0.2 Hz, all the wave energy is dissipated. In contrast, at T0 + 3h30′, T1, T1 + 2h, tidal flow reverts back and is oriented to the northeast. That induces a reduction of wave energy due to wave-current interactions (Fig. 9d, e, f). The level of energy is maximum around 0.09 Hz. At T0 − 30′ and T0 + 1h30′, wave energy is two times higher for the wind sea than at the other time points. Wind forcing being applied to the wave model every 6 hours, waves at T0 − 30′, T0, T0 + 1h30′ and T0 + 3h30′ are not re-energized by wind and hence had lost energy over

time. The wind intensity easing a little bit after 6 a.m. and therefore the wave energy for Run D sligthly decreases with a maximum value around 20 m^2/Hz. The results of Run C, including the effects of currents and water level on waves, show a reduction in wave energy mainly for the swell, leading to have similar levels of energy for both swell and wind-sea parts at T1+2h (Fig. 9f).

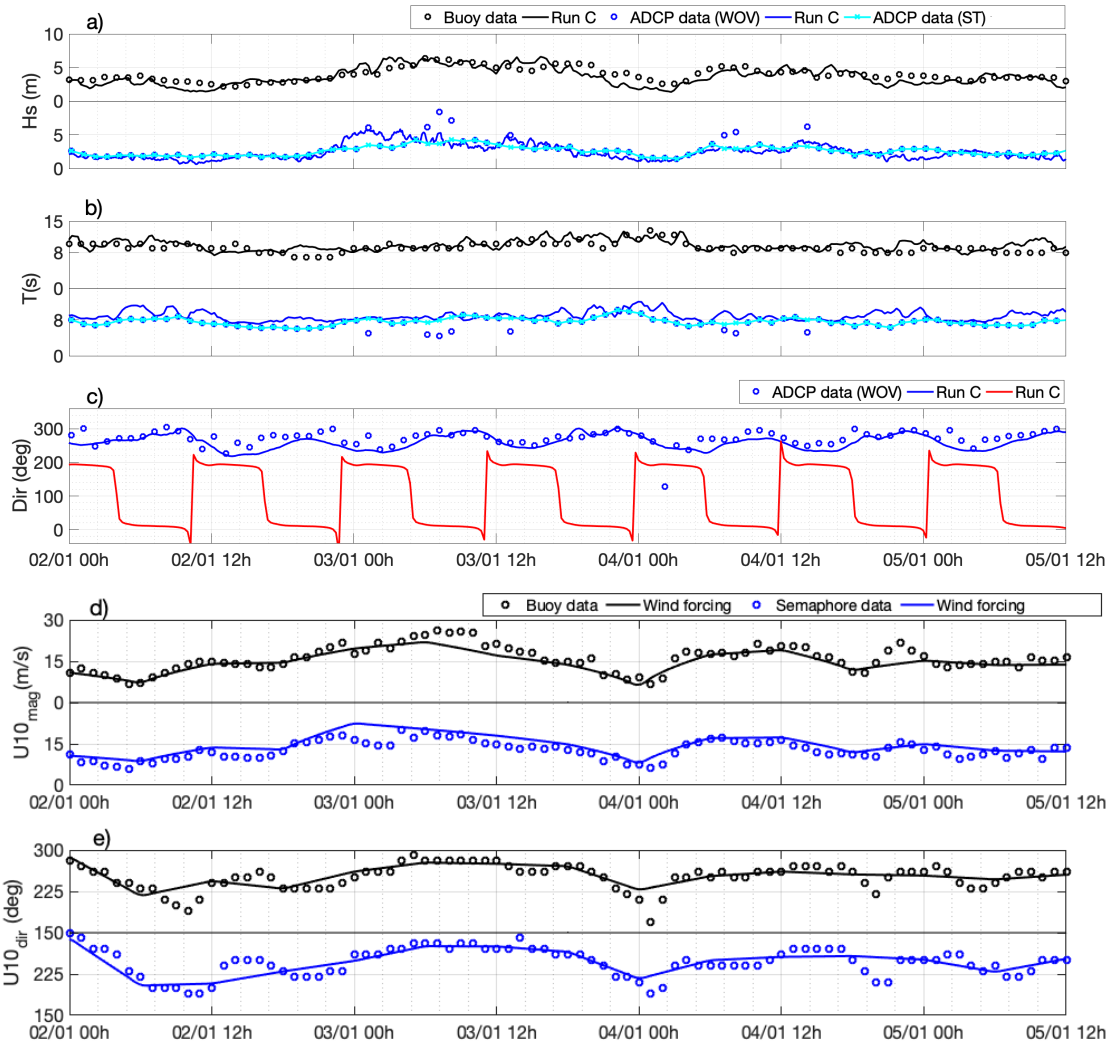

FIGURE 4: Data of buoy 62103 (black circles) against absolute wave bulk parameters of Run C (black line) for significant wave height (a), wave period (b), magnitude (d) and direction (e) of the wind velocity at 10-m height (from ALADIN). ADCP data, processed using wave orbital velocity (blue circles) and surface tracking (light blue crosses) methods, against absolute wave bulk parameters (blue line) of Run C for significant wave height (a), wave period (b) and wave direction (c). Goury Semaphore data (blue circles) against the ALADIN numerical wind forcing (blue line) for magnitude (d) and direction (e) of wind at 10-m height. (c) Current direction is drawn in red line. All data and model results are plotted over time.

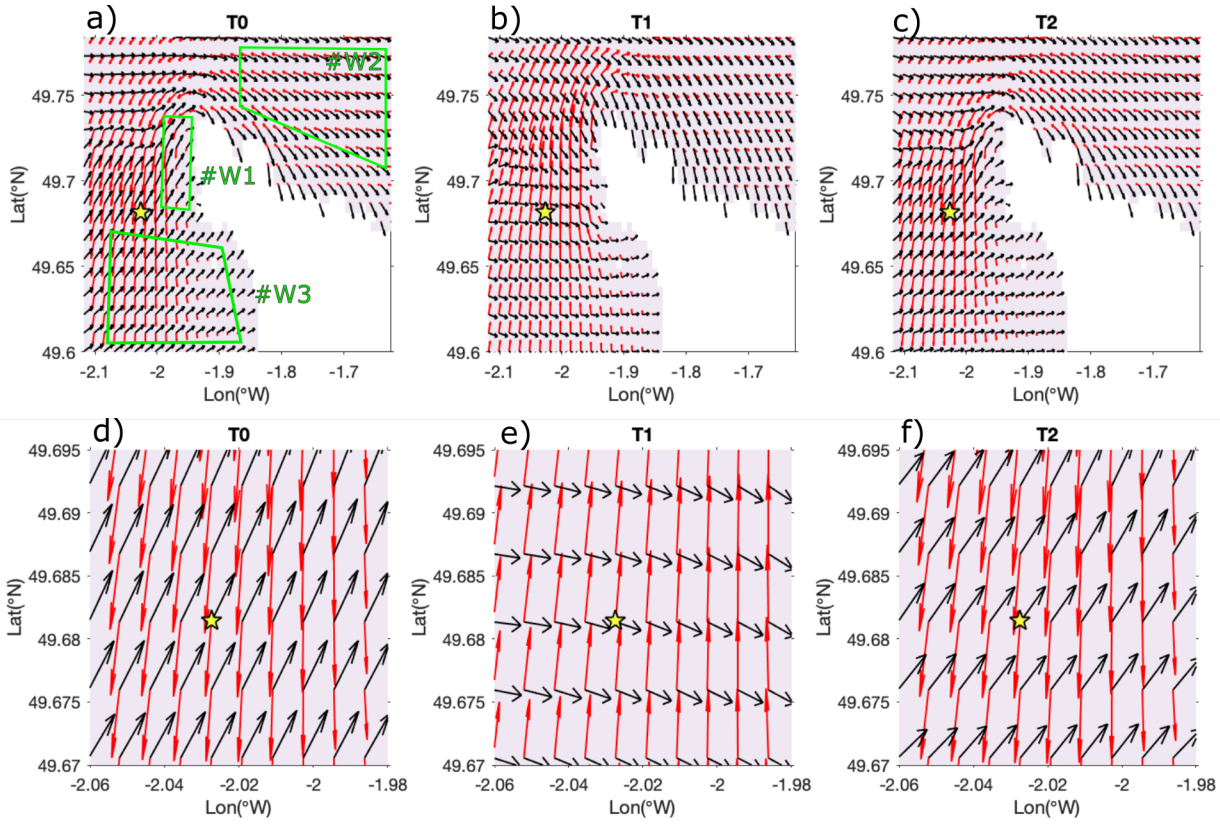

FIGURE 5: First row (a,b,c) : wave (black arrows) and current (red arrows) directions drawn each 2 grid points at T0 (a, low tide), T1 (b, high tide) and T2 (c, low tide). ADCP position is marked by a yellow star while the #W1, #W2 and #W3 areas are represented by green polygons. Second row (d,e,f) : Same legend as for the first row but for a zoom around the ADCP position where vectors are plotted every grid points.

	Hs (b/m)	**Hs (a/m)**	**T (b/m)**	**T (a/m)**	**Uw (b/m)**	**Uw (s/m)**	**Uwd (b/m)**	**Uwd (s/m)**
R^2	0.93	0.92	0.97	0.97	0.96	0.95	–	–
NRMSE	0.24	0.18	0.26	0.33	0.13	0.16	0.12	0.14
PBIAS	7.42	-1.78	5.06	-3.82	-9.22	14.59	1.10	1.10
RMSE	1.04	0.80	1.61	1.18	2.84	2.82	21.10	21.10

TABLE 2: Statistics (R^2, NRMSE, PBIAS, RMSE) calculated using Eq. (2), (3), (4), (5) related to the comparison between buoy data and model (label : b/m), ADCP data and model (label : a/m), Goury semaphore data and model (s/m). Statistics for significant wave height (Hs), wave period (T), magnitude (Uw) and direction (Uwd) of the wind velocity at 10-m height are presented.

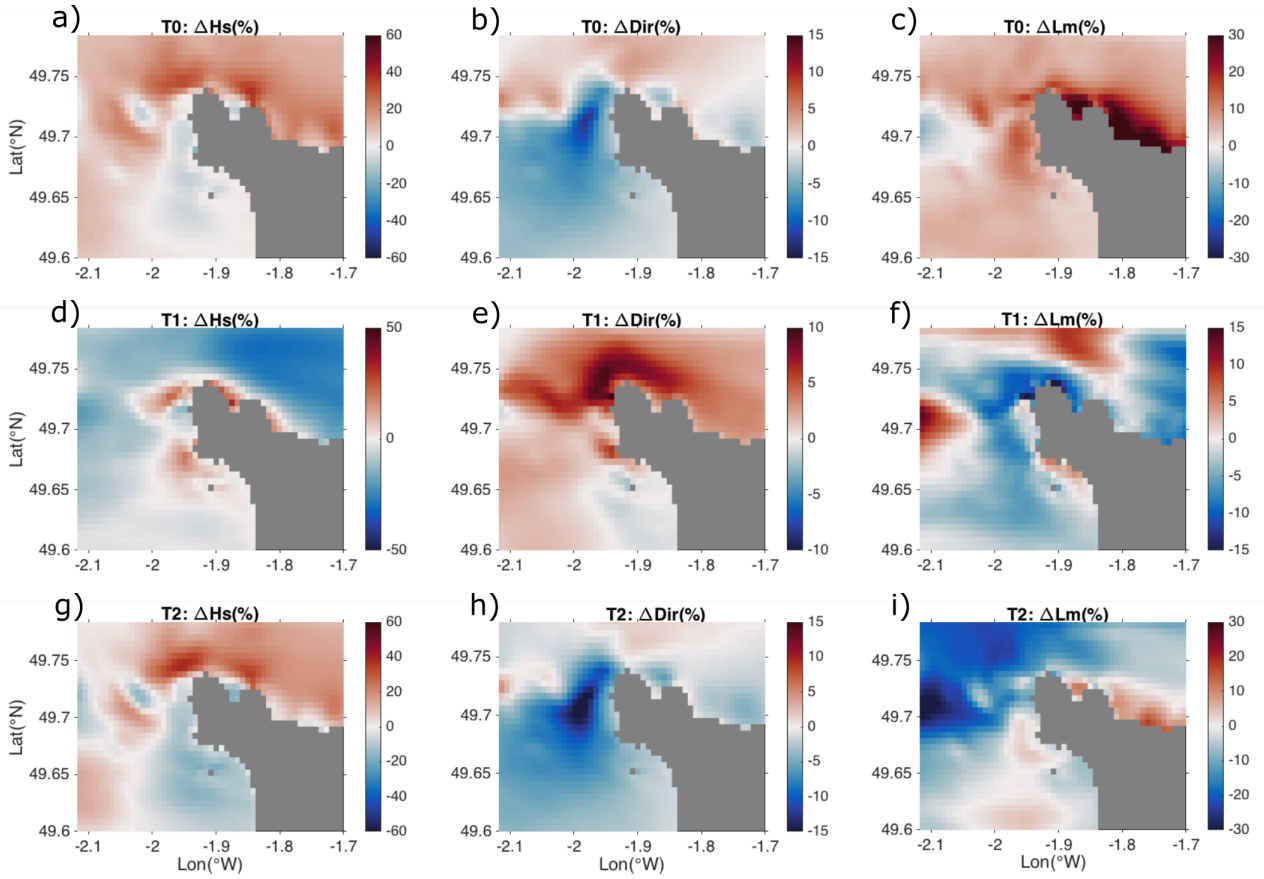

370

FIGURE 6: Relative differences for the relative bulk parameters from WWIII computed between Run C (with current and water level effects on waves) and Run D (without current and water level effects on waves). Positive values represent an overestimation of Run C relative to Run D. Three time points : T0 (low tide, first row : a, b, c), T1 (high tide, second row : d, e, f) and T2 (low tide, third row : g, h, i) are presented. Differences concern three bulk parameters : significant wave height (first column : a, d, g), mean wave direction (second column : b, e, h) and mean wavelength (third column : c, f, i).

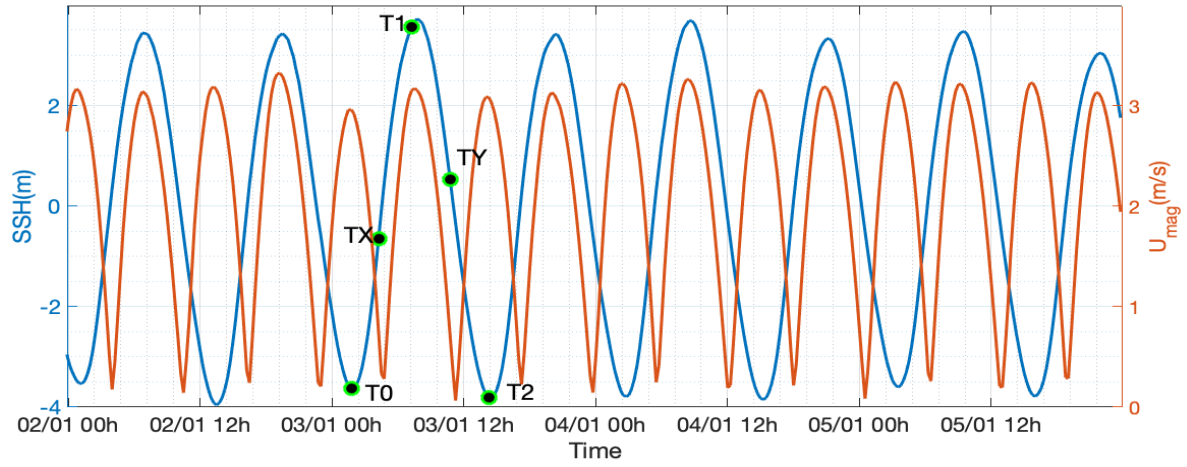

371

FIGURE 7: Time series at ADCP location computed by Run C for sea surface elevation (blue line) and velocity magnitude of the flow (red line) with marks at T0 (3/01, 1 :15 a.m., low tide), T2 (3/01, 7 :15 a.m., low tide), T1 (3/01, 2 :15 p.m., high tide), TX (3/01, 4 :15 a.m.) and TY (03/01, 10 :45 a.m.).

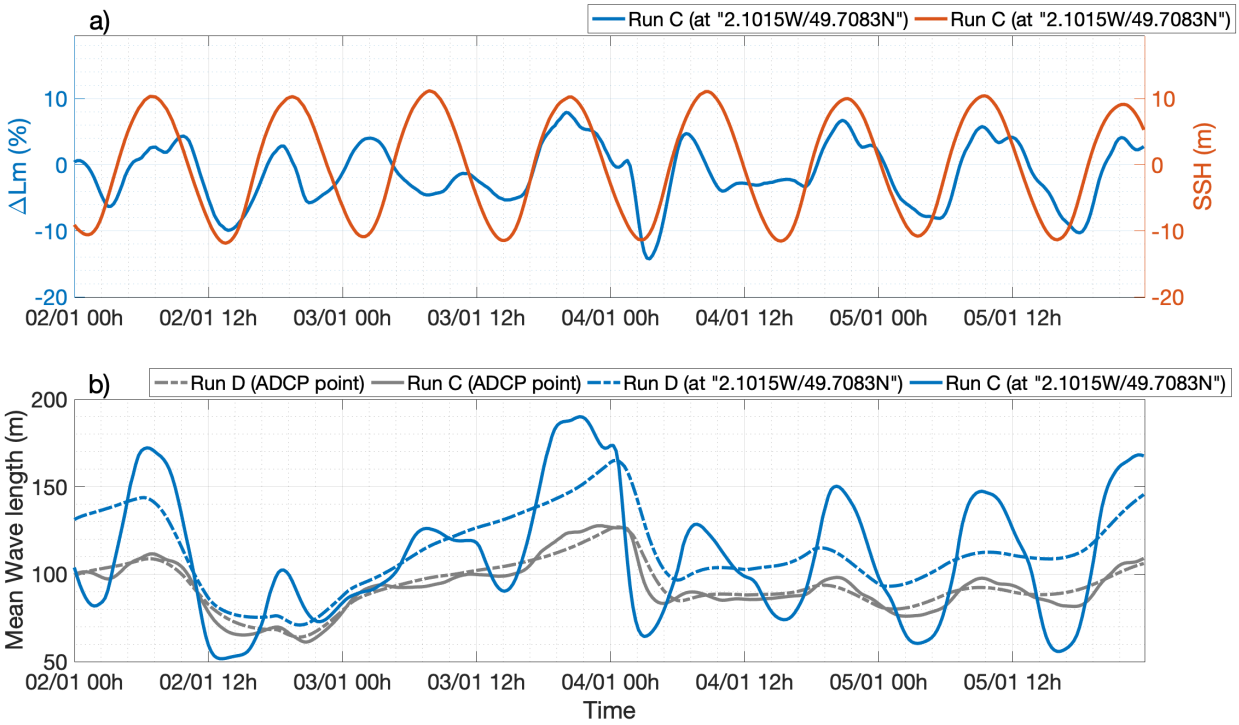

372

FIGURE 8: (a) Time evolution of the sea surface height (SSH, red solid line) and of the relative difference for the mean wavelength (ΔL_m, blue solid line) for the Run C at 2.1015W/49.7083N. (b) Time series of the mean wavelength for Run C (with current and water level effects on waves) at the ADCP position (gray solid line) and at 2.1015W, 49.7083N (blue solid line). Times series for Run D (without current and water level effects on waves) at the ADCP position (gray dashed line) and at 2.1015W, 49.7083N (blue dashed line).

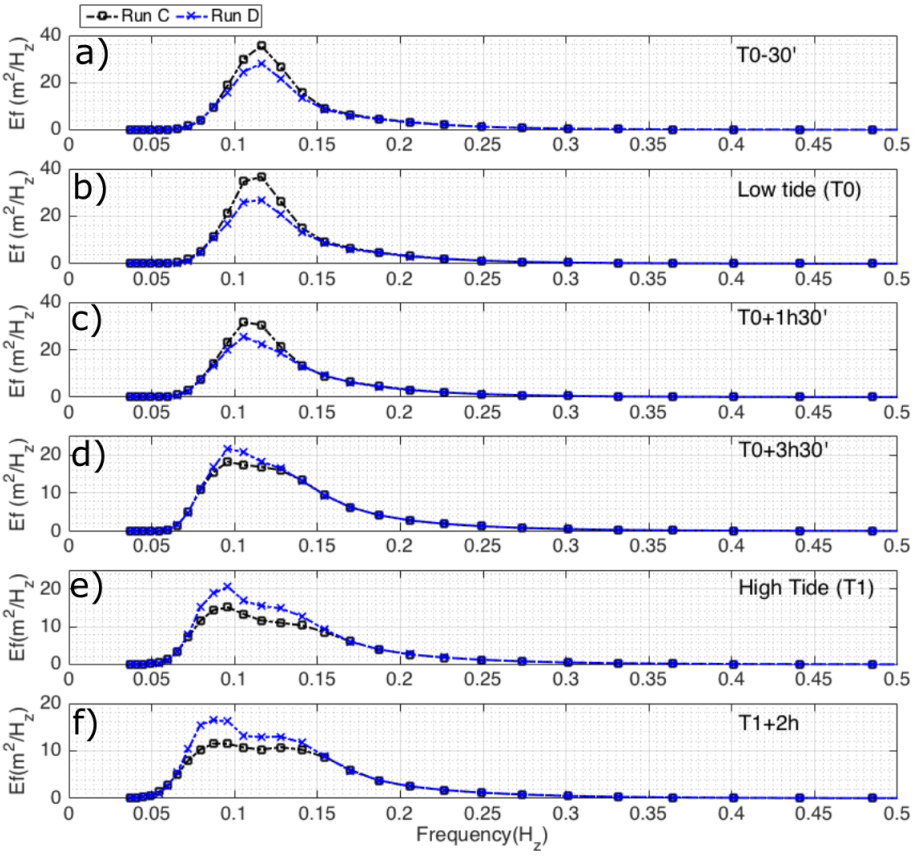

373 FIGURE 9: Relative frequency-wave energy spectra over the tidal cycle computed by WWIII. Model results for Run C (with current and water level effects on waves, black line with dots) and Run D (without current and water level effects on waves, blue line with crosses) are presented for different time points : (a) T0-30', (b) T0, (c) T0+1h30', (d) T0+3h30', (e) T1 and (f) T1+2h. The vertical scale of graphs a), b), c) differ from graphs d), e) and f).

374 *b. Flow characteristics and tidal stream energy*

375 In this section, a validation step is first performed using ADCP data for flow velocity.
376 Then, wave effects on the current are assessed and discussed as well as the changes in the
377 flow caused by the modification of the wave field by both current and water level. This study
378 concerns a given geographical area (1.6°W to 2.1°W ; 49.68°N to 49.78°N) that includes the
379 locations of the future tidal farms and ADCP point (Fig. 1).

1) Validation step : numerical results vs measurements

The coupled model has been already tested against ADCP data for Alderney Race in Bennis et al. (2020) for moderate hydrodynamic conditions in terms of sea states and tide. Despite the successful validation with excellent scores for R^2 and PBIAS in Bennis et al. (2020), an additional step of comparison is necessary to evaluate the model performances during these special conditions (storm event and spring tide).

The statistics of performance were better for the moderate conditions studied in Bennis et al. (2020) than in the present case. To support this assertion, we can compare cases with tide only (Run B, Table 4, vs Run 10 in Bennis et al. (2020)) and cases with tide, winds and waves (Run C, Table 5, vs Run 6 in Bennis et al. (2020)). Dispersion of the data is slightly worse in the pure tide case than in the previous study with a R^2 decreasing from 0.98 to 0.95, but still remains an excellent score. NRMSE is modified a quit a bit from 0.09 in Bennis et al. (2020) to 0.15 here. PBIAS is now around 10% whereas it was around 3% previously. For the case with all forcing, R^2 and NRMSE are almost unchanged between both time periods. In contrast, PBIAS has varied from about 2% to 6% now, which is an excellent score as defined in Section 2c. Discrepancies between the two sets of results have several origins. First, the simulations presented here use an horizontal resolution about 5-fold coarser than in simulations of Bennis et al. (2020) (600-m vs 120-m of horizontal resolution). This lower resolution acts as a spatial filter and smooths the computed current and sea surface height, with a reduction of their intensities as well as a mitigation of the gradients. Moreover, the location of the numerical ADCP point is slightly different from the real, leading to loss of precision due to sub-grid scale effects. Second, the particular event (Eleanor's storm and spring tide) makes more difficult the measurements and can affect their accuracy. In particular, the strong aeration of the flow ascribed to breaking waves disturbs the recording and the processing of the data. Here, the statistics computed at different depths (25m to 2m) and their means (Tables 3, 4, 5) show a great improvement when the wave effects are activated : Run A and B, computed without wave effects, have a PBIAS around 10%, while for Run C, where wave effects were taken into account, PBIAS is around 5.6%. So, accounting for wave effects has decreased PBIAS by a factor of 1.78.

	25 m	**20 m**	**15 m**	**10 m**	**8.5 m**	**6 m**	**2 m**	**MEAN**
R^2	0.95	0.95	0.95	0.95	0.94	0.95	0.96	0.95
NRMSE	0.15	0.15	0.15	0.15	0.16	0.15	0.13	0.15
PBIAS	10.17	11.06	10.94	10.90	9.60	10.02	8.00	10.09
RMSE	0.44	0.43	0.42	0.39	0.40	0.35	0.27	0.38

TABLE 3: Statistical parameters for **Run A** (with tide and wind effects) computed for the velocity magnitude on the basis of model and data results. Columns refer to different water depths.

	25 m	**20 m**	**15 m**	**10 m**	**8.5 m**	**6 m**	**2 m**	**MEAN**
R^2	0.95	0.95	0.95	0.95	0.94	0.95	0.95	0.95
NRMSE	0.15	0.16	0.16	0.16	0.16	0.16	0.14	0.16
PBIAS	10.02	10.82	10.60	10.45	9.13	9.53	7.58	9.73
RMSE	0.46	0.45	0.43	0.39	0.41	0.36	0.28	0.40

TABLE 4: Same legend as Table 3 but for **Run B** (with tide effects).

	25 m	**20 m**	**15 m**	**10 m**	**8.5 m**	**6 m**	**2 m**	**MEAN**
R^2	0.96	0.96	0.96	0.96	0.95	0.96	0.97	0.96
NRMSE	0.13	0.13	0.13	0.13	0.14	0.13	0.12	0.13
PBIAS	6.65	7.15	6.93	6.70	5.42	5.39	1.04	5.61
RMSE	0.39	0.38	0.36	0.34	0.36	0.31	0.24	0.34

TABLE 5: Same legend as Table 3 but for **Run C** (with tide, wind and wave effects).

Time series of the velocity magnitude over the depth are presented in Fig. 10. Numerical results for Run A, B and C, are compared to data. Three time periods (TP1, TP2 and TP3) are particularly studied (Fig. 12). They have been chosen for their different wind conditions (wind speed is greater than $15\,\mathrm{m.s^{-1}}$ for TP1 and TP3 and smaller than $15\,\mathrm{m.s^{-1}}$ for TP2).

Flow velocity ranges from $0.15\,\mathrm{m.s^{-1}}$ to $3.1\,\mathrm{m.s^{-1}}$ in the dataset. A tidal asymmetry is observed, as reported in the bibliography, with a more intense flood flow (about 3%) compared to the ebb flow. However, the study of the velocity profiles of the pure tidal case (Fig. 10b) and of the case with waves (Fig. 10c) highlights that wave effects affect this asymmetry by reducing the ebb flow velocity. This reduction is clearly visible in the dataset during the TP1 and TP3 time periods, where the wind velocity at 10-m height is greater than $15\,\mathrm{m.s^{-1}}$ (Fig. 4d). The peak velocity of the TP1 ebb flow is around $2.7\,\mathrm{m.s^{-1}}$ whereas the one related to the TP1 flood tide is around $3.1\,\mathrm{m.s^{-1}}$. So, the peak velocity is 13% weaker for ebb than for flood. Note that the ebb flow velocity is also reduced by 11% during TP3, where wind velocity is around $15\,\mathrm{m.s^{-1}}$. A decrease of 13% in the current intensity led to a tidal stream energy (Eq. (7)) fall of about 30% (Fig. 11). In contrast, the peak velocity for periods of low wind ($U_{10} \leq 15\,\mathrm{m.s^{-1}}$), like for TP2, is smaller by 3% for the ebb in comparison to the flood, which is in agreement with the bibliography.

Wave effects are partly transmitted to the water column by the vertical mixing (Fig. 12c), which is increased or decreased depending on the hydrodynamic conditions (Fig. 13). A strong increase (up to $0.25\,m^2.s^{-1}$) is observed during TP1 due to the strong wind and particularly affects the ebb flow because of the angle between the current and wave directions of propagation. In Fig. 15a, we observe at T0 (03/01 at 1 :45 a.m., TP1 ebb tide) that current propagates against waves at the ADCP point. This causes intense wave breaking leading to an injection of TKE in the water column. This additional turbulent source increases the vertical mixing and produces a reduction in the velocity magnitude. For the TP1 flood tide, vertical mixing is lesser enhanced due to a perpendicular direction of propagation between waves and current.

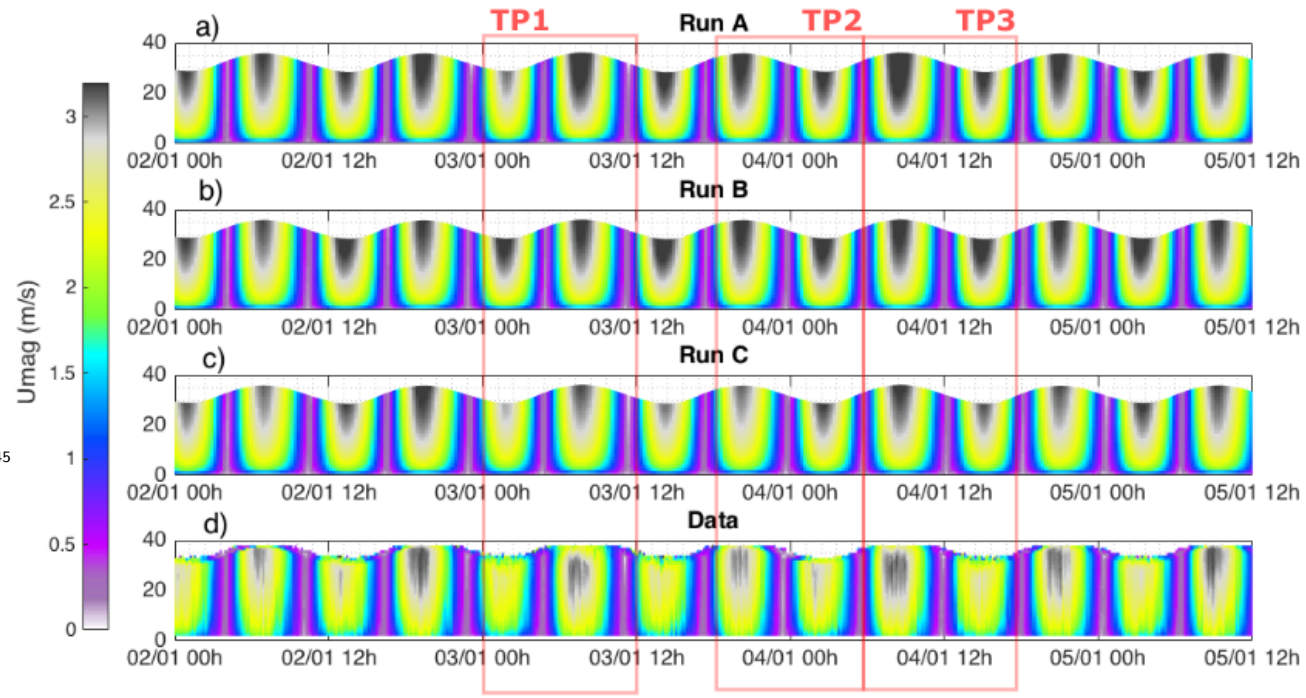

FIGURE 10: Time series of the flow velocity magnitude over the depth at the ADCP location for the model (a,b,c) and for in-situ measurements (d). (a) Run A : simulation with tide and wind effects, (b) Run B : simulation with tide effets, (c) Run C : simulation with tide, wind and wave effects.

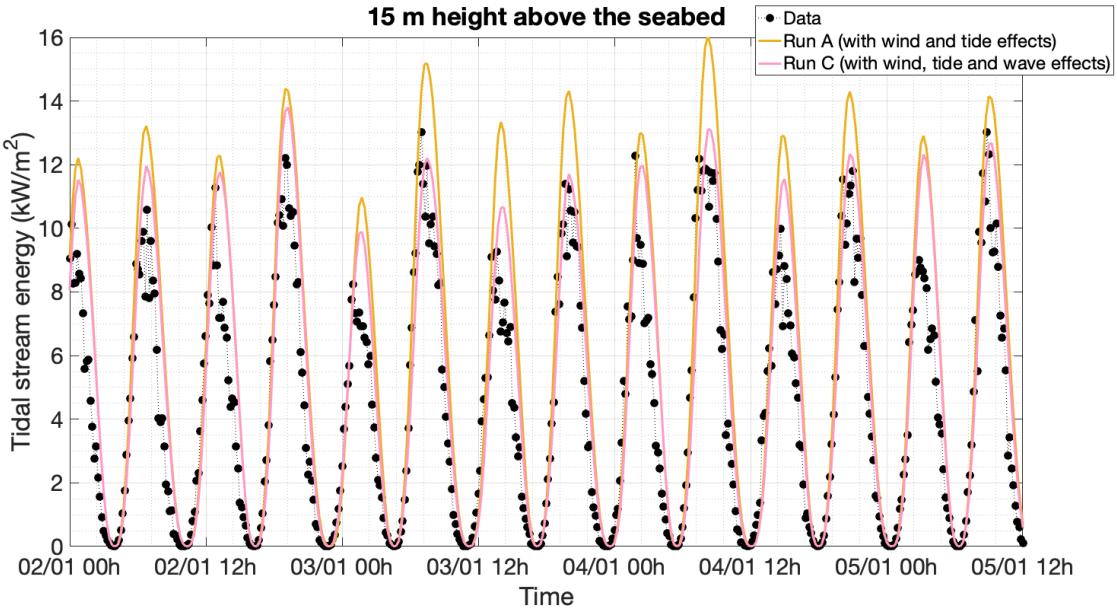

FIGURE 11: Time series of the tidal stream energy at 15 m depth at the ADCP location for the model (Run A in yellow and Run C in magenta) and for in-situ measurements (black circles).

Vertical mixing is not the only one effect modifying the vertical structure of the flow velocity. Our coupled model, using the vortex force formalism of Ardhuin et al. (2008) and Bennis et al. (2011), treats wave effects as being an assemblage of the vortex force and the Bernoulli head gradient. These terms are presented in Fig. 12a, d. We observe that the vortex force reachs its maximum values during the ebb phase (up to $2.10^{-5}\,\mathrm{m.s^{-2}}$) and is enhanced for strong winds (e.g. TP1). Moreover, its action is located in the half upper of the water column. As the vortex force depends on the Stokes drift velocity, it is interesting to see that this velocity (Fig. 12b) follows similar behaviors than the vortex force (Fig. 12a). The magnitude of Stokes drift is the highest for TP1 and reachs $0.2\,\mathrm{m.s^{-1}}$ near the surface. The gradient of the Bernoulli head at the surface also acts on the flow and is presented in Fig.12d. Values are maximum during TP1 and TP3, where waves are the highest and so the pressure exerted on the water column is the strongest. In addition, as explained and shown in Bennis et al. (2020), the bottom friction is enhanced by waves and leads to reduce the flow velocity along the water column, without change in the vertical shear. This effect partly explains why the flow velocity for Run C (with waves) is weaker than for Run A and Run B (Fig. 10). Finally, vertical profile of the flow velocity at four time points (T0 : 3/01 at 1 :45 a.m., TX : 03/01 at 4 :15 a.m., T1 : 03/01 at 7 :15 a.m., TY : 03/01 at 10 :45 a.m.) for which the current dynamic is discussed in sections 3a and 3b.2 are presented in Fig. 14. Numerical results are improved by the inclusion of wave effects in simulations (Run C) in comparison with the results of Run A : both intensity and shape of the flow velocity are coherent with

467 the data. However, some discrepancies are still noticeable, particularly at the T0 time point.
468 This could be explained by the spatial resolution of 600m, which acts as a spatial filter.

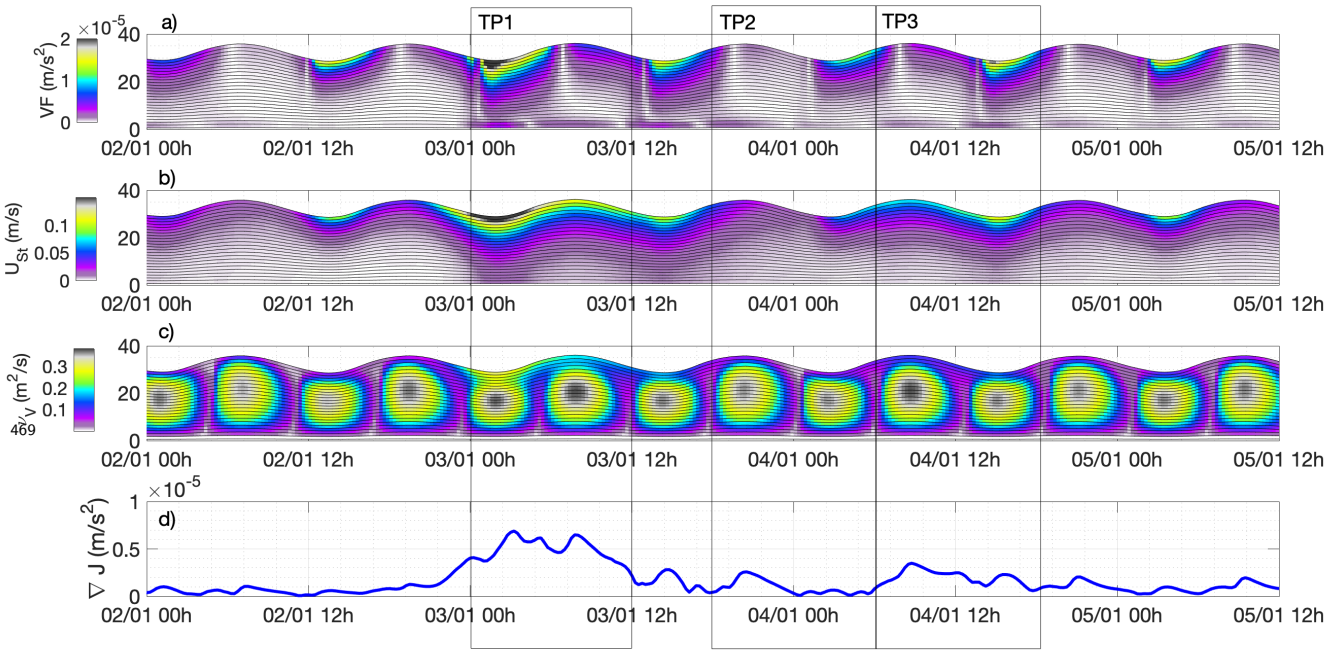

469

FIGURE 12: Time series over the depth at the ADCP location related to the vortex force (a), the magnitude of the horizontal Stokes drift (b), the vertical turbulent viscosity (c). Time evolution of the Bernoulli head gradient at the surface (d). Black lines represent the vertical discretization (25 sigma levels).

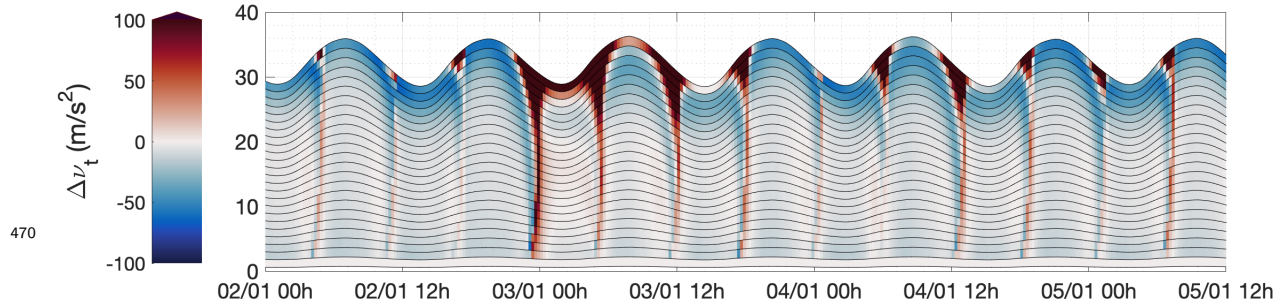

470

FIGURE 13: Relative difference (Eq. (6)) for the vertical viscosity over depth and time between Run C (with wave effects) and Run A (without wave effects) at the ADCP location. Positive values represent an overestimation of Run C relative to Run A.

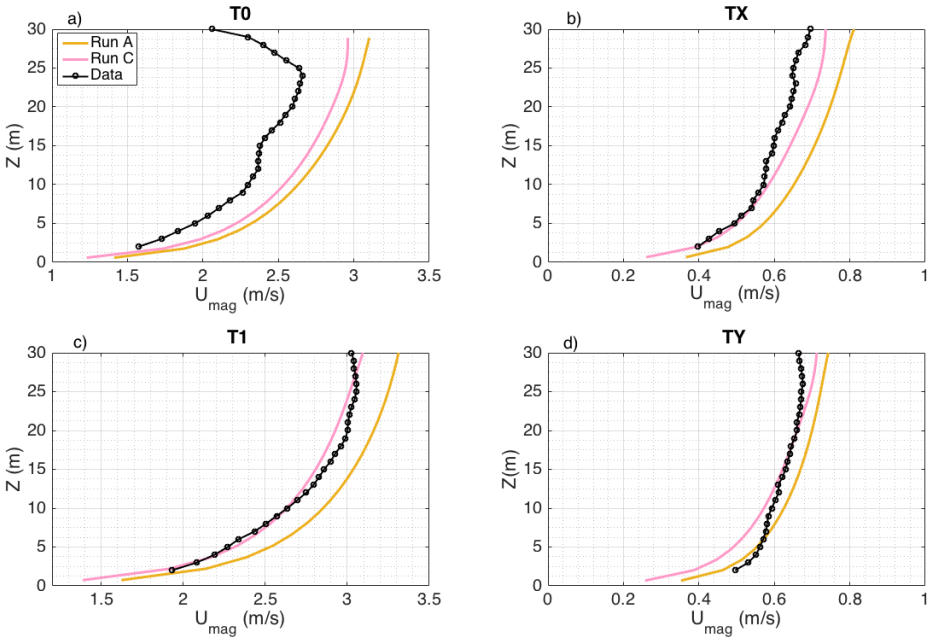

471

FIGURE 14: Magnitude of the flow velocity at ADCP location over the depth at T0 (a, low tide), TX (b, low tide slack), T1 (c, high tide) and TY (d, high tide slack) for Run A (yellow solid line ; with tide and wind effects), Run C (magenta solid line ; with tide, wind and wave effects) and ADCP data (black line with dots).

472 2) WAVE EFFECTS ON CURRENT

473 To analyze and comment the wave effects on the hydrodynamic as well as to understand
474 how current and water level effects on waves affect current by a feedback mechanism, we
475 define two different zones (Fig. 15b) : i) Area #1 located off the French northern coast and,
476 ii) Area #2 located off the Cotentin cape including a part of Alderney Race.

477 The surface flow velocity characteristics (magnitude and direction) are presented in Fig.
478 15 at T0 (a), TX (b), T1 (c) and TY (d) time points. Between T0 and TX, the flow flows
479 towards the South-West due to the ebb tide. In contrast, the flow motion is oriented towards
480 the North-East at T1 and TY ascribed to the flood tide. T0 and T1 occur at high tide and the
481 magnitude of the flow velocity reaches $4\,\mathrm{m.s^{-1}}$ in the Area #2 (Alderney Race). Velocities
482 are weaker at TX and TY due to slack tide events with a maximum value of $1.5\,\mathrm{m.s^{-1}}$.
483 The mean wave direction is also shown in Fig. 15 (black arrows). In Area #2 ocean waves
484 propagates from West to East with a deviation towards the North at T0 and TX, while they
485 are deflected towards the South at T1 and TY. This change in wave direction is caused by a
486 modification of the wind direction, and by the refraction by currents in smaller proportions,
487 as shown in Fig. 4c. In Area #1, waves travel towards the South-East for all time points. We

note different angles (θ_{wc}) between the flow and wave direction of propagation, that range from 0° to 180°. In Area #1, waves and current are opposite ($\theta_{wc} \geq 160°$) at T0 and TX, while they are oriented in the same direction ($\theta_{wc} \leq 20°$) at T1. The wave-current dynamic at T1 is more complicated due to a turbulent structure located near the coast and for which the flow velocity reachs 1.5 m.s^{-1}. The flow direction is drived by this turbulent structure and turns over 360°. It becomes opposite to the wave direction at the centre of the turbulent structure. As tidal converters will be implemented inside the Area #2, it is also relevant to analyze the related hydrodynamic. In this area, where tidal currents are the strongest in the Western Europe, waves and current directions are perpendicular most of the time or opposite as shown in Fig. 15 and 5. This fact makes difficult the understanding of the wave-current interactions. Indeed, the response of the flow is known and clear for waves following the current and for waves encountering an opposite current (e.g. Groeneweg and Klopman 1998), but it is more complex for waves perpendicular to the current.

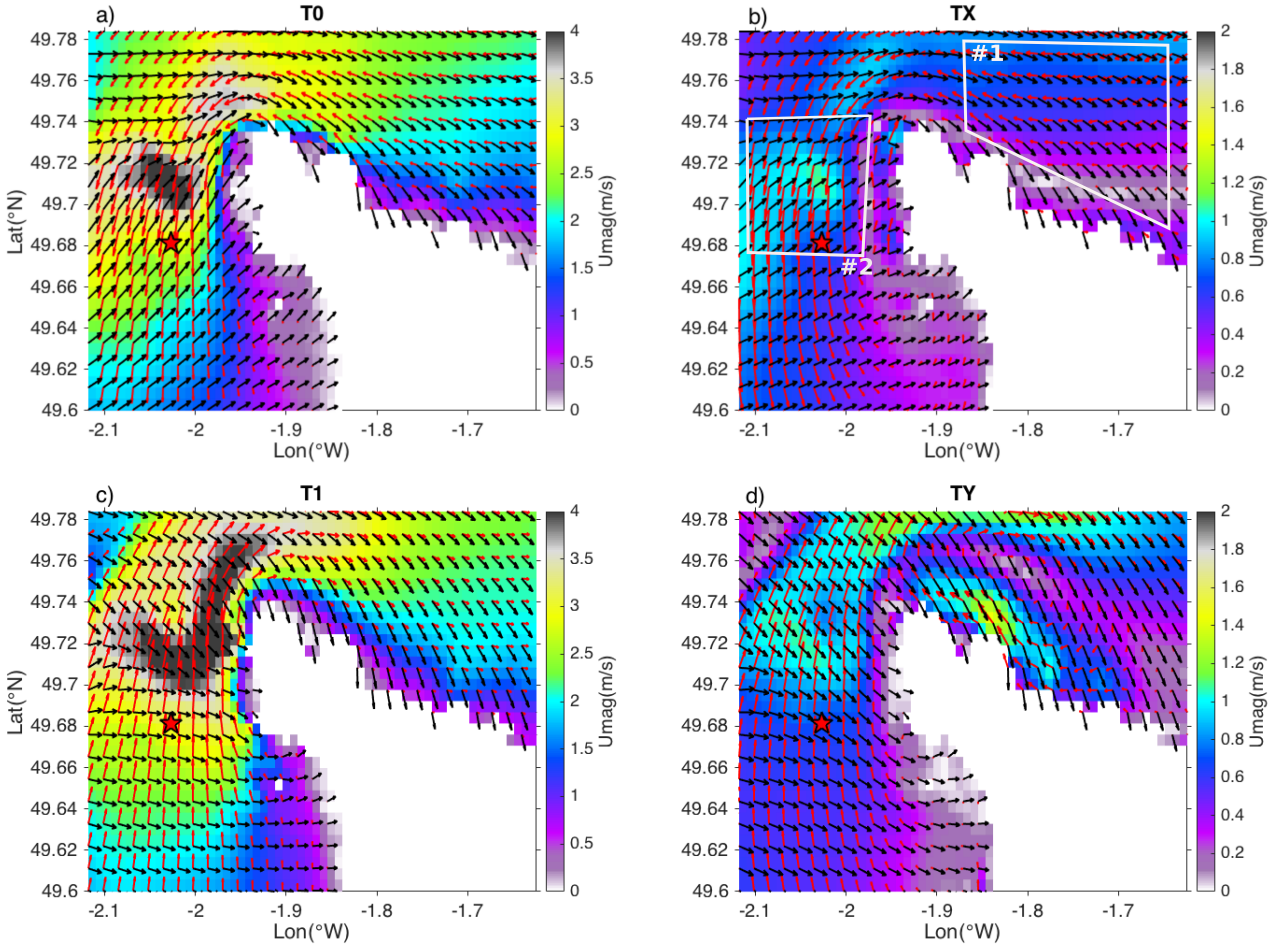

FIGURE 15: Magnitude (in color) and direction of the surface flow (red arrows) velocity and mean wave direction (black arrows) at T0 (a, low tide), TX (b, low tide slack), T1 (c, high tide), TY (d, high tide slack). ADCP location is marked with a red-black pentagram.

Wave effects on the near surface and bottom hydrodynamic are presented in Fig. 16 thanks to the absolute difference (ΔU_{wc}) for the flow velocity magnitude between Run C (with tide, wind and wave effects) and Run A (with tide and wind effects) results. As changes are similar at T0 and TX, only the T0 case is shown (Fig. 16a,d). Please note that positive values (in red) of ΔU_{wc} represent an increase of the flow velocity. For the Area #1, the flow velocity is strongly increased ($\Delta U_{wc} \leq 1\,\mathrm{m.s^{-1}}$) at T0 because waves propagate against current (Fig. 15). Current and water level effects on waves also contribute to this increase (Fig. 17 ; more details hereafter). In contrast, the flow velocity is reduced ($\Delta U_{wc} \geq -0.8\,\mathrm{m.s^{-1}}$) at T1 because waves and current travel in the same direction. Near the coast, a smaller area is concerned by a higher current ($\Delta U_{wc} \leq 0.15\,\mathrm{m.s^{-1}}$) ascribed to sub-grid scale effects that change the directions of propagation. At TY, two different behaviors are observed due to the turbulent structure : i) ΔU_{wc} is positive, representing an increase of the flow velocity, where waves and current are opposite and, ii) ΔU_{wc} is negative, representing a decrease of the flow velocity, off the turbulent structure where waves follow the current direction of propagation (Fig. 16c, top-right corner). Differences between Fig. 16c and 16f show that the turbulent structure is a three-dimensional with an higher intensity near the surface than near the bottom. Therefore, the flow direction is less deflected by the turbulent structure near the bottom and θ_{wc} remains small, so that the flow velocity is reduced ($\Delta U_{wc} \leq 0$). The hydrodynamic in Area #2 is also impacted by wave effects although the strong intensity of current. At T0, TY and T1, occurring at high tide, ($|\Delta U_{wc}|$) reachs $1\,\mathrm{m.s^{-1}}$. At T0, the flow is accelerated by the wave effects because $\theta_{wc} \geq 110°$. At T1, the flow decelerates under the wave action ascribed to a θ_{wc} smaller than 90°. At TY, wave direction is perpendicular to the current direction and a reduction of the flow velocity is observed. At the limit between Area #1 and Area #2, a modification of the response of the flow to the wave effects appeared, with an acceleration of the flow velocity in Area #1 while the velocity is reduced in #2. That is due to the turbulent structure which deviated the flow direction and change the wave-current interactions.

Overall, the wave impacts on the flow affect in the same way (reduction/acceleration) the surface flow (Fig. 16a,b,c) and the near-bottom flow (Fig. 16d,e,f), with more intense effects near the surface since waves propagate at the surface. Even if the flow response is found to be mainly ascribed to the angle between the wave and current directions of propagation according to Groeneweg and Klopman (1998), the effects of the enhancement of the bottom friction by waves should not be ignored. As shown in Bennis et al. (2020), the modification of bottom friction by waves generates a decrease of the flow velocity on the entire water column. So, when the flow velocity is decelerated or accelerated by waves, it is necessary to consider a possible reduction due to bottom friction in the changes.

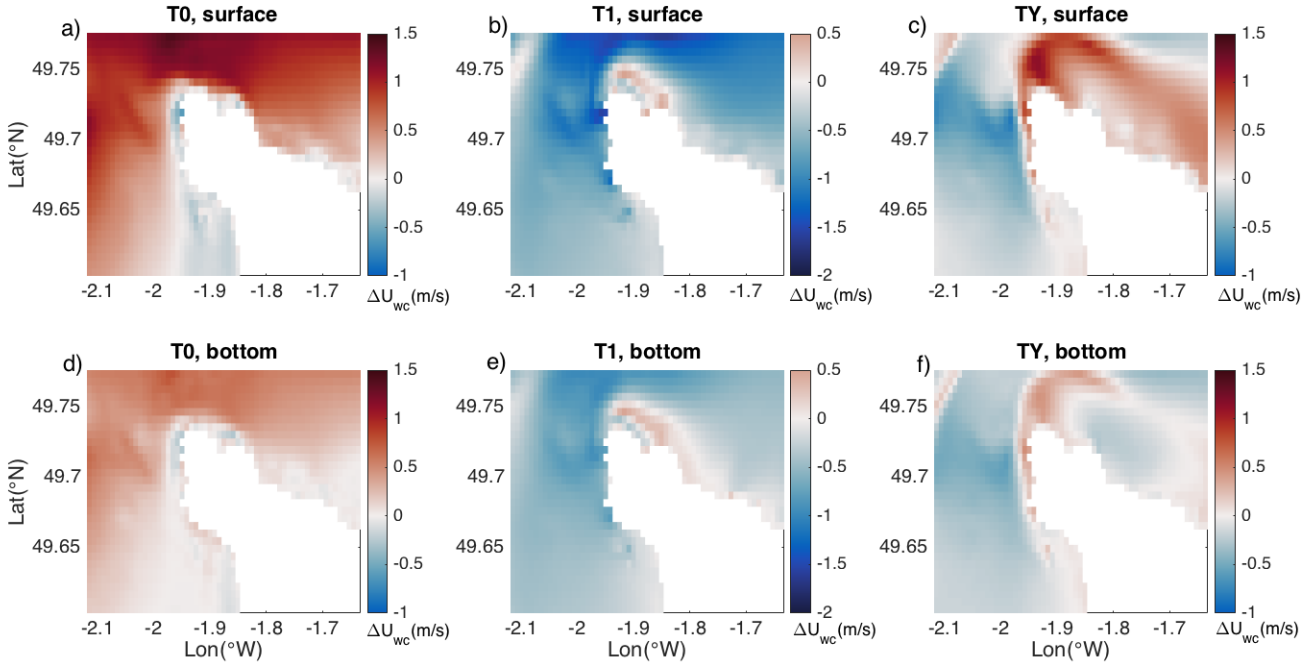

FIGURE 16: Absolute difference (ΔU_{wc}) between simulations with (Run C) and without (Run A) wave effects for the velocity magnitude near the surface (first row) and the bottom (second row) at T0 (a, d, low tide), T1 (b, e, high tide) and TY (c, f, high tide slack).

The impacts on the flow of the changes in the wave field due to current and water level effects are presented in Fig. 17. The absolute difference (ΔU_c) between Run C (two-way, with current and water level effects on waves) and Run D (one-way, without current and water level effects on waves) results is used for the analysis. Please note that positive values (in red) of ΔU_c refer to an increase of the velocity magnitude ascribed to the modifications of the wave field. In Area #1, waves and current are opposite at T0 and TX. A decrease ($\Delta U_c \leq 0.14\,\mathrm{m.s^{-1}}$ at TX and $\Delta U_c \leq 0.1\,\mathrm{m.s^{-1}}$ at T0) of the magnitude of the flow velocity is induced by the modification of the wave forcing terms due to the wave refraction by current, as observed for rip currents flowing in the opposite direction from the wave direction (e.g. Bennis et al. 2016; Weir et al. 2011). At T1, a slight increase (few centimeters per second), which is almost negligible, is caused by the current and water level effects on waves. In Area #2, at T0 and T1 occurring at high tide, the strong current significantly affects the wave field and so produces high variation in the flow velocity reaching $0.2\,\mathrm{m.s^{-1}}$. At TX, where currents are weak (low tide), changes in flow velocity are negligible ($\Delta U_c \leq 0.05\,\mathrm{m.s^{-1}}$). For the three time points in Area #2, current effects on waves cause an acceleration of the flow which is maximum near the surface and slows down over the depth. Near the bottom, the flow is almost unchanged (Fig. 17d,e,f).

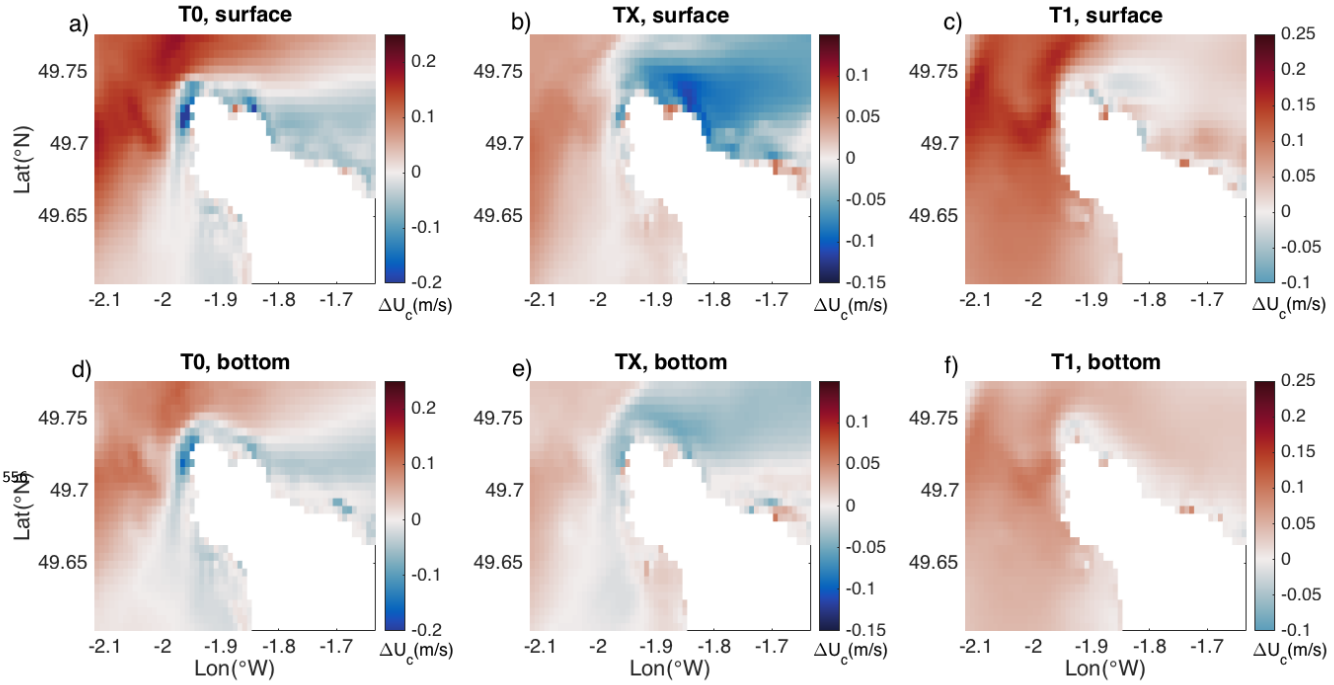

FIGURE 17: Absolute difference (ΔU_c) computed between simulations with wave effects in two-way (Run C, with current and water level effects on waves) and in one-way (Run D, without current and water level effects on waves) for the velocity magnitude. Near-surface (first row) and -bottom (second row) flow at T0 (a, d, low tide), TX (b, e, low tide slack) and T1 (d, f, high tide).

The tidal stream energy is an useful indicator for tidal companies to predict the energy potential and its formulation is :

$$P = \frac{1}{2}\rho \widehat{U}_{mag}^3, \tag{7}$$

where $\widehat{U}_{mag}$ is the magnitude of the quasi-Eulerian flow velocity and ρ is the water density.

The tidal energy converters for Alderney Race are rather high : the turbines of Hydro-Quest and Simec-Atlantis, anchored to the seabed, have a height around 22 m. Due to this design, the tidal stream energy at 15-m depth is representative of the extracted power by the converters. The absolute difference (ΔP) between Run C (with wave effects) and Run A (without wave effects) is used for the analysis below. Please note that positive values (in red) of (ΔP) refer to an increase of P due to wave effects. As the tidal stream energy (P) is based on the flow velocity, its behavior at 15-m depth in Alderney Race (Area #2) is similar to the current behavior, as shown in Fig. 18. At T0, P is increased up to 25 kW.m^{-2} due to high tide and the related wave-current interactions. In the bibliography (e.g. Guillou et al. 2016; Lewis et al. 2017), authors have reported that wave effects produce a reduction in the tidal

stream energy because the studies were carried out in cases where wave-current interactions mainly influence the bottom friction. Here, the wave enhancement of the bottom friction is not the major effect because of the special hydrodynamic conditions (i.e. the Eleanor's storm and spring tide). It is interesting to show cases, such as at T0 and TY (not presented here), where the tidal stream energy is increased by waves. In contrast, about 35 $\mathrm{kW.m^{-2}}$ are lost at T1. Maximum changes in P are located in the main vein of the current, with a reduction by a factor of 2 at T0 and a 1.7-fold increase at T1.

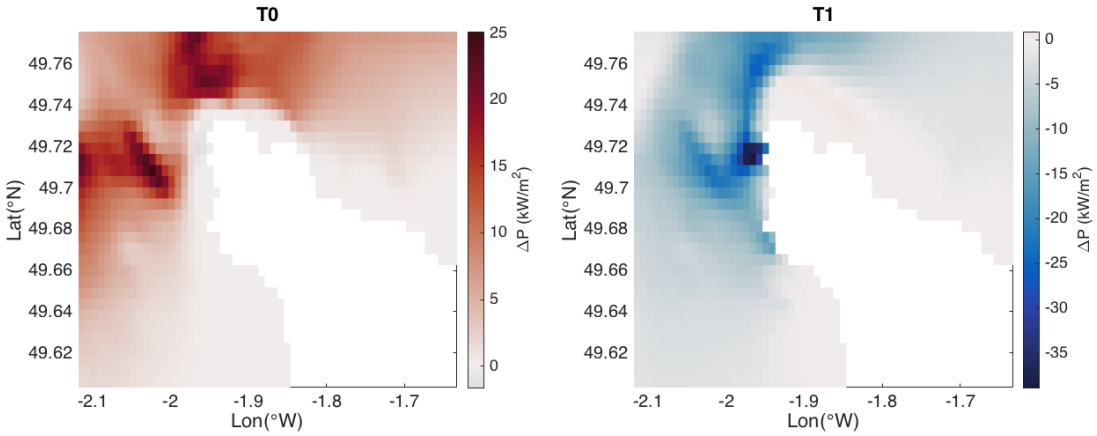

FIGURE 18: Absolute difference for the tidal stream energy (ΔP) between simulations with (Run C) and without (Run A) wave effects for the tidal stream energy at 15-m depth and at T0 (left panel, low tide) and T1 (right panel, high tide).

4. Conclusions

The impact of a winter storm during spring tide on the hydrodynamic and tidal stream energy in AR was studied for the first time here. The excellent scores obtained for the validation of the numerical model with *in-situ* data have revealed the good capacity of the coupled numerical model, MARS-WWIII, for simulating the hydrodynamic for this time period. However, data are limited in geographic and temporal scope and it is possible that lower scores are obtained at other locations. In the future, comparisons with spatialized data (e. g. HF radar data) will be carried out for completing the validation of the model. Our results have shown that ocean waves during the Eleanor's storm have significantly affected the flow although they occurred during spring tide. With such tidal conditions, one may have though that the wave effects on the flow would have been negligible. This study has proven the contrary. In that case, ocean waves has changed the vertical structure of the tidal current and also its intensity. The main effect was a strong variation in the tidal asymmetry due to waves. Ebb flow was found 13% lower than the flood flow for the

present storm conditions instead of 3% for calm conditions. That is an important result for industry because it means that the energy extracted from the ebb flow is reduced by 30%. Although the tidal companies plan to stop the converters during extreme events such as storms, they are interested in knowing such information to define when to shut down the turbines. Otherwise, the wave field is found to be strongly influenced by the tidal current as already reported in Bennis et al. (2020), showing that coupled wave-current numerical simulations are required for AR. This study was performed during spring tide because ADCP data were available. In the future, further works are necessary to generalize these results by investigating different hydrodynamic conditions such as a storm during neap tide or a storm with different characteristics.

Acknowledgments

Authors are supported by the HYD2M project (ANR-10-IEED-0006-07) funded by the program called "Investissements d'avenir" for the building of France Energies Marines. Authors are grateful to F. Ardhuin for providing the WAVEWATCH-III forcing fields. Results acquired with the Ifremer MARS software. Simulations have benefited of the computing facilities of CRIANN.

Références

Allen, J. I., J. T. Hold, J. Blackford, and R. Proctor, 2007a : Error quantification of a high-resolution coupled hydrodynamic-ecosystem coastal-ocean model : Part 2. Chlorophyll-a, nutrients and SPM. *J. Mar. Sys.*, **68**, 381–401.

Allen, J. I., P. J. Sommerfield, and F. J. Guilbert, 2007b : Quantifying uncertainty in high-resolution coupled hydrodynamic-ecosystem models. *J. Mar. Sys.*, **64**, 3–14.

Ardhuin, F., N. Rascle, and K. A. Belibassakis, 2008 : Explicit wave-averaged primitive equations using a generalized Lagrangian mean. *Ocean Modelling*, **20**, 35–60.

Ardhuin, F., et al., 2012 : Numerical wave modeling in conditions with strong currents : dissipation, refraction and relative wind. *J. Phys. Oceanogr.*, **42**, 2010–2112.

Bailly du Bois, P., F. Dumas, M. Morillon, L. Furgerot, C. Voiseux, E. Poizot, Y. Méar, and A.-C. Bennis, 2020 : The Alderney Race : general hydrodynamic and particular features. *Phil. Trans. R. Soc. A*, **378**, 20190 492.

Bailly du Bois, P., F. Dumas, L. Solier, and C. Voiseux, 2012 : In-situ database toolbox

for short-term dispersion model validation in macro-tidal seas, application for 2D-model. *Continental Shelf Research*, **36**, 63–82.

Bennis, A.-C., F. Adong, M. Boutet, and F. Dumas, 2021 : LANS-α turbulence modeling for coastal sea : An application to Alderney Race. *Journal of Computational Physics*, **432**, 110 155.

Bennis, A.-C., F. Ardhuin, and F. Dumas, 2011 : On the coupling of wave and three-dimensional circulation models : Choice of theoretical framework, practical implementation and adiabatic tests. *Ocean Modelling*, **40**, 260–272.

Bennis, A.-C., P. Bailly Du Bois, F. Dumas, C. Lathuilière, F. Adong, and J.-F. Filipot, 2018 : Towards a realistic numerical modelling of wave-current-turbulence interactions in Alderney Race. *2018 OCEANS - MTS/IEEE Kobe Techno-Oceans (OTO)*, IEEE, 1–7.

Bennis, A.-C., F. Dumas, F. Ardhuin, and B. Blanke, 2014 : Mixing parameterization : impacts on rip currents and wave set-up. *Ocean Engineering*, **42**, 213–227.

Bennis, A.-C., F. Dumas, and B. Blanke, 2016 : Modulation of wave-current interactions by horizontal mixing and spatial resolution. *Ocean Modelling*, **99**, 75–85.

Bennis, A.-C., L. Furgerot, P. B. D. Bois, F. Dumas, T. Odaka, C. Lathuilière, and J.-F. Filipot, 2020 : Numerical modelling of three-dimensional wave-current interactions in complex environment : application to Alderney Race. *Applied Ocean Research*, **95**, 102 021.

Boudiere, E., C. Maisondieu, F. Ardhuin, M. Accensi, L. Pineau-Guillou, and J. Lepesqueur, 2013 : A suitable metocean hindcast database for the design of marine energy converters. *International Journal of Marine Energy*, **3**, 40–52.

Bourgoin, A., S. Guillou, J. Thiébot, and R. Ata, 2020 : Turbulence characterization at a tidal energy site using large-eddy simulations : case of the Alderney Race. *Phil. Trans. R. Soc. A.*, **378**, 20190 499.

Coles, D. S., L. S. Blunden, and A. S., 2017 : Assessment of the energy extraction potential at tidal sites around the channel islands. *Energy*, **124**, 171–186.

Dauvin, J.-C., 2019 : *The English Channel : La Manche*, 153–188. Cambridge, MA : Academic Press Published.

Draycott, S., J. Steynor, T. Davey, and D. M. Ingram, 2018 : Isolating incident and reflected wave spectra in the presence of current. *Coastal Engineering Journal*, **60 (1)**, 39–50.

Furgerot, L., G. Lopez, A. Sentchev, P. Bailly Du Bois, M. Morillon, E. Poizot, Y. Méar, and A.-C. Bennis, 2020 : One year measurement in Alderney Race : what did we learn ? *Phil. Trans. R. Soc. A.*, **378**, 20190 625.

Furgerot, L., Y. Poprawski, M. Violet, E. Poizot, P. Bailly Du Bois, M.Morillon, and Y. Méar, 2019 : High-resolution bathymetry of the Alderney Race and its geological and sedimentological description (Raz Blanchard, northwest France). *Journal of Maps*, **15**, 708–719.

Groeneweg, J. and G. Klopman, 1998 : Changes in the mean velocity profiles in the combined wave-current motion described in GLM formulation. *J. Fluid Mech.*, **370**, 271–296.

Guillou, N., 2017 : Modelling effects of tidal currents on waves at a tidal stream energy site. *Renewable Energy*, **114**, 180–190.

Guillou, N., G. Chapalain, and S. P. Neill, 2016 : The influence of waves on the tidal kinetic energy site. *Applied Energy*, **180**, 402–415.

Hashemi, M., S. Neill, P. Robins, A. Davies, and M. Lewis, 2015 : Effects of waves on the tidal energy resource at a planned tidal stream array. *Renewable Energy*, **75**, 626–639.

Kumar, N., G. Voulgaris, J. C. Warner, and M. Olabarrieta, 2012 : Implementation of the vortex force formalism in the coupled ocean-atmosphere-wave-sediment transport (COAWST) modeling system for inner shelf and surf zone applications. *Ocean Modelling*, **47**, 65–95.

Lazure, P. and F. Dumas, 2008 : An external-internal mode coupling for a 3d hydrodynamical model for applications at regional scale (MARS). *Adv. Water Resources*, **31**, 233–250.

Leroy, R. and B. Simon, 2003 : Réalisation et validation d'un modèle de marée en Manche et dans le golfe de Gascogne - Application à la réalisation d'un nouveau programme de réduction de sondages bathymétriques.

Lewis, M., S. Neill, P. Robins, M. Hashemi, and S. Ward, 2017 : Characteristics of the velocity profile at tidal-stream energy sites. *Renewable Energy*, **114**, 258–272.

Lewis, M. J., S. P. Neill, P. E. Robins, and M. R. Hashemi, 2015 : Resource assessment for future generations of tidal-stream energy arrays. *Energy*, **83**, 403–415.

Lopez, G., A.-C. Bennis, Y. Barbin, A. Sentchev, L. Benoit, and L. Marié, 2020 : Surface hydrodynamics in the Alderney Race from HF Radar measurements and 3D modelling. *Phil. Trans. R. Soc. A.*, **378**, 20190 494.

683 Lopez, G., et al., 2018 : Hydrodynamics of the alderney race : Hf radar wave measurements.
684 *Proceeding of the International Conference on Ocean Energy, France*, 1–6.

685 Marchesiello, P., R. Benshila, R. Almar, Y. Uchiyama, J. C. McWilliams, and A. Shchepetkin,
686 2015 : On tridimensional rip current modeling. *Ocean Modelling*, **96**, 36–48.

687 Marechal, D., 2004 : A soil-based approach to rainfall-runoff modelling in un- gauged catch-
688 ments for england and wales. Ph.D. thesis, University of Cranfield, UK.

689 McWilliams, J. C., J. M. Restrepo, and E. M. Lane, 2004 : An asymptotic theory for the
690 interaction of waves and currents in coastal waters. *J. Fluid Mech.*, **511**, 135–178.

691 Mercier, P., M. Grondeau, S. Guillou, J. Thiébot, and E. Poizot, 2020 : Numerical study of
692 the turbulent eddies generated by the seabed roughness. case study at a tidal power site.
693 *Applied Ocean Research*, **97**, 102 082.

694 Mercier, P., et al., 2021 : Turbulence measurements : An assessment of acoustic doppler
695 current profiler accuracy in rough environment. *Ocean Engineering*, **226**, 108 819.

696 Raoux, A., I. Robin, J.-P. Pezy, A.-C. Bennis, and J.-C. Dauvin, 2021 : Multi-disciplinary
697 and multi-scale assessment of marine renewable energy structure in a tidal system. *Journal*
698 *of Energy and Power Technology*, **3**, 1–16.

699 RDI, 2017 : Waves primer : wave measurements and the RDI ADCP waves array technique.
700 1–33 pp.

701 Salomon, J.-C. and M. Breton, 1993 : An atlas of long-term currents in the channel. *Ocea-*
702 *nologica Acta*, **16 (5-6)**, 439–448.

703 Strong, B., B. Brumley, E. Terray, and G. Stone, 2000 : Performance of ADCP-Derived
704 Directional Wave Spectra and Comparison with Other Independent Measurements. *2000*
705 *MTS/IEE Oceans Conference, Providence*, IEEE, 1195–1203.

706 Thiébaut, M., J.-F. Filipot, C. Maisondieu, G. Damblans, R. Duarte, E. Droniou, N. Cha-
707 plain, and S. Guillou, 2020 : A comprehensive assessment of turbulence at a tidal-stream
708 energy site influenced by wind-generated ocean waves. *Energy*, **191**, 116 550.

709 Tolman, H. L. and al., 2014 : User manual and system documentation of WAVEWATCH-
710 III^{TM} version 4.18. Tech. Rep. 282, NOAA/NWS/NCEP/MMAB.

711 Uchiyama, Y., J. C. McWilliams, and A. F. Shchepetkin, 2010 : Wave-current interaction
712 in oceanic circulation model with a vortex-force formalism Application to the surf zone.
713 *Ocean Modelling*, **34**, 16–35.

Valcke, S., T. Craig, and L. Coquart, 2015 : OASIS3-MCT User Guide. Tech. rep., CERFACS.

Walstra, D. J. R., J. Roelvink, and J. Groeneweg, 2000 : Calculation of wave-driven currents in a 3D mean flow model. *Proceedings of the 27th international conference on coastal engineering, Sydney*, ASCE, Vol. 2, 1050–1063.

Wang, P. and J. Sheng, 2018 : Tidal modulation of surface gravity waves in the Gulf of Maine. *Journal of Physical Oceanography*, **48 (10)**, 2305 – 2323.

Weir, B., Y. Uchiyama, E. M. Lane, J. M. Restrepo, and J. C. McWilliams, 2011 : A vortex force analysis of the interaction of rip currents and surface gravity waves. *J. Geophys. Res.*, **116**, C05 001.